Microwave Heating of Water and Cyclohexane: A Molecular Dynamics Study

by

Victor Hugo Malamace da Silva

A thesis submitted in partial fulfillment of the requirements for the degree of

Master of Science

in
Chemical Engineering

Department of Chemical and Materials Engineering
University of Alberta

Abstract

The oil sands of Western Canada are among the most abundant and economically important unconventional petroleum resources. Hydrocarbon extraction from oil sands is conducted using warm water or *in situ* technologies that face considerable environmental challenges. Oil sands can also be valorized using the alternative method of non-aqueous extraction (NAE). However, NAE faces the challenge of solvent removal from post-extraction gangue. Microwave heating (MWH) has been explored as an energy-efficient approach for recovering the residual solvent from the gangue. In this work, the MWH of solvent-water systems present in the pores of NAE gangue was studied using molecular dynamics simulations. In particular, the temperatures changes of water and the NAE solvent cyclohexane were investigated under an external electric field, representative of MWH. The two liquids were simulated in monophasic and biphasic unit cells, applying an electric field with strengths of 0.01 V/nm and 3 V/nm and frequencies of 915 MHz, 2.45 GHz, and 100 GHz under constant pressure or constant volume condition. It was found that the applied electric field heated up the water molecules, due to their high dipole moment, but did not heat the nonpolar cyclohexane molecules that were transparent to the electric field. The simulations of biphasic systems showed that the temperatures of both water and cyclohexane increased, indicating that water was heated by the electric field and its thermal energy was transferred to the cyclohexane. Among the electric field strengths and frequencies tested, only the strength of 3 V/nm provided sufficient heating for each frequency applied, while the strength of 0.01 V/nm was too weak and the frequency of 100 GHz caused rapid heating. The heating mechanism was further explored using the rotational autocorrelation function and diffusion coefficient. It was found that the MWH increased both rotational motion and diffusion. The temperature increase and molecular motion were correlated to explain the microwave heating and thermal transfer. The study provides a possible explanation of the solvent recovery from the gangue generated from NAE using MWH.

Preface

This thesis is an original work by Victor Hugo Malamace da Silva. No part of this thesis has been previously published.

Acknowledgments

For the work performed during this master's degree, I thank primarily my parents, Isis and Marcos, for all the emotional, financial, and spiritual support they have given me during all these years. I thank my partner Nieva for the love and support during this and the future steps of my career.

The work is also dedicated to my supervisors Professor Phillip Choi and Professor Qi Liu for all the wise advice during my degree. Additionally, to Dr. Stanislav Stoyanov, who besides being a supervisor throughout these years, is also a friend and family in Canada. Special thanks to my previous supervisors Dr. Glaucio Braga Ferreira and Dr. Jose Walkimar for all the opportunities that allowed me to start these master's degree. The work is dedicated to the computational chemistry team at Universidade Federal Fluminense for all the friendship and knowledge that helped me get where I am.

To my friends Alex, Arthur, Gabriel and Xu for the immense friendship despite the distance and all the friends I have met during these two years in Canada. This thesis was only possible by your everyday support and jokes, especially my Brazilian friends Filipe, Jessika, Gabriel and Larissa.

This thesis is also dedicated to all who, wherever they are, will always look for us during this journey, especially my grandparents Aridio, Celia e Maria de Lourdes, my uncle Marcelo and my friend Sugaya.

For the development of this work, the group wants to acknowledge the funding from Future Energy Systems, Imperial Oil, the Chemical and Materials Engineering Department and the Faculty of Graduate Studies and Research. This work was done in collaboration with Dr. S. R. Stoyanov from Natural Resources Canada.

Table of Contents

List of Tables

List of Figures

1 Introduction

1.1 Background

An increasing demand for energy worldwide, coupled with the scalability challenges of green energy results, in a growing need for fossil fuels (Biello, 2011). Currently, petroleum is the most important fossil fuel worldwide. Petroleum resources can be generally classified as conventional and unconventional. Conventional petroleum is found in reservoirs trapped by several rock formations with high porosity, following impermeable rocks. The impermeable rock formation ensures that the oil is kept on site and can be extracted with minimal stimulation and at a lower cost. The conventional petroleum extraction can be done offshore, by a drillship or a semi-submersible platform, or onshore by using vertical wellbores. Unconventional petroleum resources can be found in low porosity rock formations, where the oil surrounds the rock and cannot be extracted by a vertical wellbore used in the conventional process. Unconventional petroleum recovery requires stimulation, such as hydraulic fracturing, heating, or other, to obtain the crude oil, which increases the extraction cost relative to the conventional process (Wang et al., 2020).

The Athabasca region in Western Canada holds the world's third largest hydrocarbon reserve (Internationale Energieagentur, 2010). Petroleum extraction from the oil sands yielded 2.8 million barrels per day in 2017, which can be refined and distributed to several industries and for the domestic use of gas (Chen and Liu, 2019). The main challenge in the commercial development of this unconventional petroleum reserve is the low hydrocarbon content. The Athabasca oil sands contain 7-12% of bitumen mixed with sand, clays, and several percent of water. At a commercial scale, bitumen is recovered from surface and deep oil sands deposits by surface mining and *in situ* processes, respectively (Butler et al., 1981).

Since 2013, *in situ* recovery by steam injection has become the primary industrial process for bitumen extraction from the Athabasca oil sands (OIL SANDS MAGAZINE, 2016; Peng et al., 2020). A representative *in situ* process, steam assisted gravity drainage (SAGD) employs two parallel wells separated by approximately 5 m, often reaching as deep as 150 to 450 m below the ground level. One well is used for the injection of steam in a deep oil reservoir and the other well is for the recovery of a produced fluid containing bitumen, water, and sand particles (Chung et al., 2011; Cui et al., 2022). The fluid produced from multiple wells is pumped to ground facilities for phase separation. The phase separation is conducted in several steps, such as free water knockout, treatments using solvents and dewatering agents, and gravity separation, in order to remove water and fines from the hydrocarbon product. Solvent addition decreases the density of the organic phase, assisting in the gravity-based separation. The use of steam to perform the oil extraction increases energy use and greenhouse gas (GHG) emissions associated with *in situ* recovery (Hristova et al., 2023).

The surface mining of oil sands is employed for deposits situated at less than 75 m from the ground level. The mined oil sands ore is crushed, added to hot water, and agitated mechanically. The produced aqueous slurry is hydro-transported to flotation-like separation vessels, where bitumen droplets liberated from the sand grains coalesce and are aerated to float. Bitumen froth is collected at the top and tailings are discharged from the bottom of the separation vessel. This process, described here in simple terms, is known as Clark hot water extraction (Clark, 1966). The mining process achieves high product recovery from high grade oil sands. The bottom residue, containing alkaline aqueous suspensions with residual bitumen and sand grains, known as tailings, is deposited in tailings ponds. The tailings ponds pose environmental challenges due to their sheer size and the time required to settle. In addition to the expansion of tailings ponds, the hot water extraction from surface mined oil sands causes extensive land disturbance and requires thermal energy, contributing to greenhouse gas

emissions (Jordaan, 2012; Lin et al., 2017). The hot water extraction process also faces a limitation in terms of the recovery of bitumen from low-grade ores and oil-wetted reservoirs. The hot water extraction efficiency decreases from 90% for high-grade ores to 60% or less for medium- and low-grade ores. Additionally, the Clark hot water extraction method is limited to water-wetted deposits, such as the Athabasca oil sands, but cannot be applied to oil-wetted oil sands, such as those found in Venezuela and Utah (OIL SANDS MAGAZINE, 2020).

Non-aqueous extraction (NAE) has been considered as an alternative to the commercial steam- and hot water-based processes for bitumen extraction (Khalkhali et al., 2022). Several techniques for a water-free extraction have been reported, such as the solvent-alone extraction (SAE) and the solvent extraction spherical agglomeration (SESA). The SAE process was initially investigated in the USA by Graham et al., aiming to improve the oil-wetted bitumen found in the region (Graham et al., 1987). This method uses an organic solvent rather than water for bitumen extraction after the mined ore has been crushed. After the crushed ore is blended with an organic solvent, a step called solvent digestion, the mixture is subjected to primary separation, where it undergoes a solid-liquid separation. The supernatants from the separation stage, which can be performed in multiple vessels, contain diluted bitumen with fine particles that are further separated by a chemical or mechanical process. The bottom stream from the separation vessels, called a wet gangue, is subjected to solvent recovery by steam stripping. The recovered solvent can be recycled for the first step of extraction. After removing the fine particles, the diluted bitumen stream is processed by distillation (Lin et al., 2017; Zhu et al., 2018). In the SESA process, the addition of solvent and a small amount of water to the oil sands are used to extract the bitumen. This method consists of bitumen separation and solvent recovery, and is often classified in literature as an SAE method (Sparks and Meadus, 1981). However, the SESA method has two features to distinguish it from other NAE methods. The water addition helps the formation of spherical agglomerates of fine particles, allowing a

more efficient extraction of bitumen and solvent. The minimized content of fines in the final bitumen-solvent product is the second characteristic of the SESA technology. Furthermore, fines agglomerates lead to a more efficient solvent recovery (Meadus et al., 1982). Researchers have investigated different properties to establish the potential organic solvents for bitumen extraction, evaluating their toxicity, bitumen recovery, economic cost, and solvent recovery. After investigation using organic solvents for the recovery of high- and low-grade ores, cyclohexane was identified as one of the best NAE solvents. The solvent selection was based on several criteria, such as the bitumen recovery and product quality, especially in comparison to the hot water extraction, which shows the high potential of NAE methods (Khalkhali et al., 2022; Wu and Dabros, 2012).

The NAE offers a significant advantage in bitumen recovery by efficiently removing heavy oil from ores of different grades and sources. This water-free process also provides dry tailings, which eliminates the environmental impact brought by the hot water process and features a low water consumption for the overall extraction. However, the NAE has presented challenges and gaps concerning its safety procedure. Since the oil sands extraction involves the use of a large amount of ore, which can present a risk due to its abrasive property, the use of organic solvent can add a risk to the operation for its explosive and toxic characteristics. Most solvents can create vapor clouds posing potential health risks to workers. The solvent recovery is presented as another challenge faced by the solvent extraction. The recovery process has often been inadequate, with a high energy demand during the distillation step to meet the minimum amount of solvent loss of 0.004% v/v, required by the Alberta Energy Regulator (Lin et al., 2017). The solvent recovery challenge associated with this high energy demand has been investigated in the literature by several researchers promoting solvent removal alternatives to distillation, such as air-drying and microwave heating; however, this challenge remains unresolved.

Microwave heating was proposed because of its selective heating and lower heat loss compared to conventional heating. The microwave is limited to the power absorption from polar materials, such as water molecules. In the NAE, water contents in the wet gangue can be responsible for conducting the microwave heating towards the other components, such as cyclohexane and residual bitumen, trapped in the sand particles. Khalkhali et al. have investigated the use of microwave heating for different samples of oil sands gangue to compare its efficiency with that of the air-drying method for the recovery of cyclohexane as the extraction solvent. The study shows the use of water as a heating agent for the microwave method, leading to more efficient drying and solvent recovery. The authors also state the use of a small amount of added water would be sufficient to improve the cyclohexane recovery (Khalkhali et al., 2022).

The wet gangue produced by NAE contains water and cyclohexane trapped in between sand grains, along with non-extracted bitumen. The interaction between trapped water and cyclohexane mentioned in experimental studies (Khalkhali et al., 2022) can be illustrated by the diagram in Figure 1-1, showing both in a biphasic system due to their immiscibility.

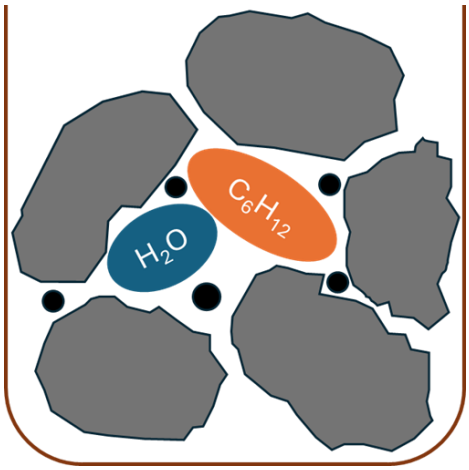

Figure 1-1 Graphic representation of wet gangue, containing sand grains in grey, bitumen in black, cyclohexane in orange and water in blue.

1.2 Microwave heating

Heating using microwaves can be applied to different industrial settings. This heating process can be used in mining, as the microwave may generate cracks in rock structures due to thermal stress (Gao et al., 2020). Additionally, applying this type of radiation to the ceramic industry allows to reduce process temperatures and produce new composites, as noted in the literature (Binner et al., 2007). Other applications are related to metallurgy, for extracting metals and removing unwanted materials from the product (Bhatt and Ghetiya, 2022). The microwave as a heat source is widely applied in the food industry, creating a reliable alternative and reducing the cost of the overall process in comparison to heat convection and conduction oven (Piyasena et al., 2003). The microwave radiation has been used for laboratory investigations as an alternative to conductive heating source for more than forty years. It presents as a faster, greener, and cheaper alternative tool for chemical reactions. This improved efficiency was stated by Leadbeater *et al.* for the synthesis of biodiesel, where microwave irradiation was applied and compared to the thermal heating of the whole solution, performed in a continuous flow and batch reactors (Leadbeater, 2014). Other studies also presented an enhanced performance using microwave as a heating source to perform organic reactions, e.g. Suzuki, Diels-Alder, hydrolysis. The heating efficiency was also investigated for several substances, including water (Hoogenboom et al., 2009). This study analyzed molecules with different organic groups and how the heating by microwave performs, finding the amount of electricity that would generate microwave irradiation, where the water, with the highest heating efficiency, presented under 50% conversion of electric energy to actual heat.

The mechanism responsible for the microwave heating of materials, such as solids, liquids, and gases, is based on the rotation of molecules' electronic dipoles generated by the oscillation of the electromagnetic field (Bonifas et al., 2007). For molecules with a permanent dipole moment, such as water, the electric field reorients the dipole moment to the direction of

the field. When a high-frequency microwave is applied (e.g., 2.45 GHz), this change cannot immediately follow the shift of the electric field, which would delay the rotation (Hoogenboom et al., 2009). The increase in the temperature is mainly caused by this delay in the rotational movement and exceeding rotational kinetic energy, which overcomes the translational and vibrational energy. This fact builds up a rotationally-excited molecule of water and The power of microwaves can also be applied to synthesize inorganic and organic compounds (Mohorič and Bren, 2020).

In the spectrum of electromagnetic radiation, the microwaves correspond to frequencies ranging from 300 MHz to 300 GHz. Internationally, the microwave equipment for household use operates at 2.45 GHz and for industrial use, it runs at 915 MHz or 2.45GHz. This limit is reserved to reduce its impact on other waves used in medical, research, and industrial equipment (Guzik et al., 2022).

Microwave heating is widely studied for various applications involving different materials. Since microwaves are electromagnetic waves, pertinent theories about microwave heating are developed based on Maxwell's equations (Barringer et al., 1994). The permittivity (ε) of a material determines how fast the material is heated when exposed to a microwave, and it is determined by its dielectric character. The permittivity is usually characterized by the complex relative permittivity (ε*) of the material that contains the real and imaginary components dielectric constant (ε') and dielectric loss factor (ε''), respectively, as expressed in Eq. 1-1.

$$\varepsilon^* = \varepsilon' - j\varepsilon'' \qquad \textit{Eq. 1-1}$$

The dielectric constant (ε') signifies the energy absorbed by the material, while the dielectric loss factor (ε'') is the loss of the input microwave energy to the form of heat, and j is the imaginary constant $\left(\sqrt{-1}\right)$ (Komarov *et al.*, 2005).

In the analysis of the heat transfer from the applied electric field to a material, the heating rate is described by Eq. 1-2. If the convective heat transfer from the system to the surrounding is negligible, Eq. 1-2 can be simplified to Eq. 1-3 (Barringer et al., 1994).

$$\frac{d\bar{T}}{dt} = \left[\frac{\bar{P}}{\rho C_p} + \frac{(T_\infty - T_0)hA}{\rho V C_p}\right] \qquad \textit{Eq. 1-2}$$

$$\frac{d\bar{T}}{dt} \approx \frac{\bar{P}}{\rho C_p} \qquad \textit{Eq. 1-3}$$

In these equations, the variables are set as t for time, h for the convective heat transfer coefficient, ρ for the density, C_p for the specific heat capacity at constant pressure. The T_0 and T_∞ refer to the initial temperature of the system and the surrounding temperature, respectively. The parameters V, A, $\bar{P}$ and $\bar{T}$ are the volume and surface area of the sample, the volumetric power absorption, and the average temperature, respectively.

The power absorbed by a material can be derived for a uniform plane wave of an electric field with a strength of E_0, as described by Eq. 1-4. In this equation, ε_0 is the free space dielectric constant, ω is the angular frequency of the electromagnetic radiation in rad/s, and E_z is the electric field distribution with its complex conjugate, E_z^*. Here, it is assumed that the dielectric properties are independent of the temperature and the power absorption is constant (Ayappa *et al*., 1992).

$$P = \frac{1}{2}\omega\varepsilon_0\varepsilon'' E_z E_z^* \qquad \textit{Eq. 1-4}$$

1.3 Molecular Dynamics Simulation

With the advance of computational technologies and theoretical knowledge of chemical behaviour, molecular dynamics (MD) has become an essential tool for many investigations related to bulk phase, polymers, reactions, and diffusion (Cheng and Yuan, 2020; English and

MacElroy, 2003a; Matsumoto and Matsuura, 2004). The MD method aims to simulate time-dependent properties and behaviours for a system of particles. The MD method is widely used in many different science sectors to provide a deeper understanding of observable phenomena (Rapaport, 2004). The MD simulations use statistical mechanics to provide a connection between the properties of a system, such as correlating temperature and pressure to energy, velocity, and position. Statistical mechanics aim to describe the macroscopic behaviour of physical systems by its microscopic properties and constituents, applying probabilistic assumptions. The statistical mechanics has as its main task to identify the different factors involved in the system to approach the equilibrium state. This approach works with statistical ensembles, which are characterized by thermodynamic variables, such as energy (E), volume (V), temperature (T), pressure (P), and number of atoms (N) (Jensen, 2017).

The MD method is usually applied to many molecules in a nanoscale unit cell to ensure a statistically significant simulation. The limitation of using a small volume comes from the computational cost and may not describe a bulk phase precisely. Since MD is a statistical mechanics method, a large sample is needed for an accurate description of the statistical analysis of properties, such as velocity, potential energy, and temperature. To overcome the precision issue and keep the simulation in a reasonable time frame, MD uses periodic boundary conditions (PBC) to extend the unit cell by copying it in all three directions (Rapaport, 2004). The PBC approach allows the simulation to reproduce the bulk phase by removing the model boundary limitation and introducing a continuous interaction among molecules. The molecule's short-range interaction with other molecules is also limited to a radius, commonly known as a cut-off radius. The Figure 1-2 illustrates the reproduction of the unit cell in PBC and the cut-off radius.

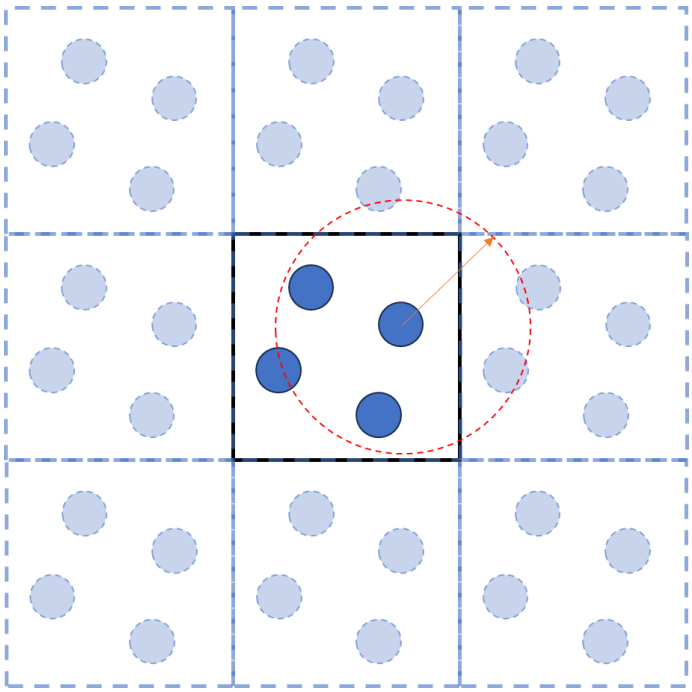

Figure 1-2 A unit cell subjected to periodic boundary conditions in two dimensions with the interaction radius shown in red.

Molecular dynamics simulations essentially integrate the Newton's equations of motion of a set of particles (atoms) in a molecular system at specific temperature and pressure and generate information such as atomic positions and velocities over a period of chosen simulation time. These atoms are treated as spherical particles that can move around the system and interact with each other. The interaction among particles and their movement are the fundaments of MD simulations. The Newton's equation of motion for a particle *i* is described by Eq. 1-5 below, where it computes the force $\boldsymbol{F}$ on the particle from the mass m and acceleration $\boldsymbol{a}$ (Fehske et al., 2008).

$$\boldsymbol{F}_i = m_i \boldsymbol{a}_i \qquad \textit{Eq. 1-5}$$

This equation can also be expressed in terms of the second time derivative of the position $\boldsymbol{r}$ of the particle (see Eq. 1-6). The force is related to the potential energy (E_{Pot}) of the particle in the gravitational field, also shown in Eq. 1-6. Knowing the force and mass of each

atom makes it possible to calculate its acceleration. The future velocity and, consequently, the future position can also be determined. The force, acceleration, velocities, and position are determined for a time interval *dt*, and are assumed to be constant during this small time interval. Once a set of positions has been determined, a new set of forces is calculated, allowing new calculations for the acceleration that is repeated for another time interval. This procedure is done for a total time *t*, established by the user (Fehske et al., 2008).

$$\boldsymbol{F}_i = m_i \boldsymbol{a}_i = m_i \frac{d^2 \boldsymbol{r}_i}{dt^2} = -\frac{dE_{Pot}}{d\boldsymbol{r}_i} \qquad \textit{Eq. 1-6}$$

At the beginning of the simulation, the velocities need to be initialized along with the atomic positions that can be found in an input. The first velocities are determined by applying the Maxwell-Boltzmann distribution for the three-dimensional velocities. This distribution can be done by multiplying the mean square velocity, given by $\sqrt{3k_bT/m}$, and Gaussian distributed random numbers, with k_b as the Boltzmann constant, m as the mass of the particles, and T as the temperature stated on the ensemble. The distribution is then applied to all directions, ensuring a total momentum of zero, leading the particle position to stay around a local minimum in energy. The temperature is consequently related to the initial velocity determined in the previous step and expressed by Eq. 1-7, where $\boldsymbol{p_i}$ is the momentum of particle $\boldsymbol{i}$, and 3N signifies the number of degrees of freedom from the system (Rapaport, 2004).

$$T = \frac{1}{3Nk_B} \langle \sum_{i=1}^{N} \frac{|\boldsymbol{p}_i|^2}{m_i} \rangle \qquad \textit{Eq. 1-7}$$

The total energy can also be expressed as the sum of the kinetic and potential energies, which will be correlated to the force applied (Eq. 1-8). As mentioned, the force of Eq. 1-6 is the parameter used to calculate the particle's acceleration. The kinetic energy can be

determined by the velocity of each particle combined with their mass, as expressed in Eq. 1-9, for $\boldsymbol{v}$ as the velocity for each *i* atom in the *x, y*, and *z* directions (Jensen, 2017).

$$E_{tot} = E_{kin} + E_{Pot} \qquad \textit{Eq. 1-8}$$

$$E_{kin} = \sum_{i=1}^{N} \frac{1}{2} m\left(\boldsymbol{v}_{x,i}^2 + \boldsymbol{v}_{y,i}^2 + \boldsymbol{v}_{z,i}^2\right) \qquad \textit{Eq. 1-9}$$

The potential energy can be decomposed into bonded and non-bonded components, typically related to the molecule geometry and the interaction between nearby atoms. Eq. 1-10 expresses the different components of the potential energy of a molecule. It contains the bond energy (E_{bond}) that is associated with the bond length and is also called the stretching energy, the angular term or bending energy (E_{angle}) that considers the change in the bond angle formed by three atoms in a molecule, the torsion energy ($E_{torsion}$) that incorporates the change on the dihedral angle of the molecule, out-of-plane bending energy (E_{oop}) that represents the energy associated with the atom's movement out of the structure plane, and the cross term among the other energies (E_{cross}). Also, there is a non-bonded interactions energy term ($E_{non\text{-}bond}$) (Jensen, 2017);

$$E_{molec} = E_{bond} + E_{angle} + E_{torsion} + E_{oop} + E_{cross} + E_{non-bond} \qquad \textit{Eq. 1-10}$$

The bond stretching energy relates to the difference between the bond length in equilibrium and the distance between the atoms at a determined simulation time. In its simplest form, the stretching energy can be described in Eq. 1-11, where *b* states the bond length at a time *t* and b_0 is the bond length in its "normal" or "equilibrium" state. In this harmonic oscillator form of the stretching energy, k_b is the force constant between both atoms.

$$E_{bond} = \sum_{bonds} \frac{1}{2} k_b (b - b_0)^2 \qquad \textit{Eq. 1-11}$$

The quadratic form of the stretching energy is widely used for most of the equilibrium geometries and sufficient for most simulations. As the representation on Eq. 1-11 is determined by a Taylor series expansion, other terms can be included for a more precise description. Another popular stretching energy expression used is the Morse stretching energy equation, as shown in Eq. 1-12. For this equation, the difference between the bond length and its equilibrium value (i.e., Δb) is incorporated in an exponential term, where D is the dissociation energy and α is a force constant (see Eq. 1-13). The Morse form of the stretching energy can be applied for a wide range of distances and converges to the dissociation energy. However, this expression has its limitations when presented with distorted structures and, for an average case, its results are close to the polynomial expression shown previously (Jensen, 2017).

$$E_{bond,Morse} = \sum_{bonds} D(1 - e^{-\alpha \Delta b})^2 \qquad \textit{Eq. 1-12}$$

$$\alpha = \sqrt{\frac{k}{2D}} \qquad \textit{Eq. 1-13}$$

The bending term represents the energy required to change the bond angle from the equilibrium angle. Similar to the stretching energy, the bending energy is also expressed by a Taylor series expansion and can be described by a quadratic equation, as shown in Eq. 1-14. To define the bending term, the equation has both angles at the equilibrium, θ_0, and at the time t, θ, and the angle force constant H_θ. The quadratic expression for the bending energy can be improved by adding a third term from the Taylor series expansion, as shown in Eq. 1-15. Adding a new term is relevant for a more accurate calculation, as Eq. 1-14 describes the energy sufficiently well for a change of 20° between the equilibrium angle, and the third term can be valid for a bond angle bending up to 70°.

$$E_{angle} = \sum_{\theta} H_{\theta}(\theta - \theta_0)^2 \qquad \textit{Eq. 1-14}$$

$$E_{angle} = \sum_{\theta} H_2(\theta - \theta_0)^2 + H_3(\theta - \theta_0)^3 \qquad \textit{Eq. 1-15}$$

The torsion energy is associated with the rotation of a bond and is determined by the position of 4 atoms, A-B-C-D, where the B-C is the bond of interest (Jensen, 2017). The dihedral angle is defined as the angle formed by two bonds, A-B and C-D. Different from the stretching and the bending energy, the torsion energy has some contribution from the non-bonding terms, and the equation that expresses $E_{torsion}$ is written by a Fourier series, as shown in Eq. 1-16. In the torsion energy equation, ϕ describes the dihedral angle, V_1 can be interpreted as the dipole-dipole interaction, V_2 is the bond conjugation, and V_3 is the steric energy. Some software also applies the torsion energy considering the Ryckaert-Bellemans function, described as a more efficient expression (Eq. 1-17), and where C_n are the Ryckaert-Bellemans constants.

$$E_{torsion} = V_1(1 + \cos\phi) + V_2(1 + \cos(2\phi)) + V_3(1 + \cos(3\phi)) \qquad \textit{Eq. 1-16}$$

$$E_{torsion} = \sum_{n=0}^{5} C_n(\cos\phi)^n \qquad \textit{Eq. 1-17}$$

In the out-of-plane movement, the energy results from the symmetry distortion, where one atom moves away from a plane established in equilibrium. This term can also be interpreted as an energy penalty for an increasing inversion barrier as a planarity or non-planarity movement. The equation to model the out-of-plane or inversion energy is also a harmonic term for the angle, as demonstrated by Eq. 1-18, with H_χ being the force constant and χ being the angle difference from the equilibrium.

$$E_{oop} = \sum_{\chi} H_{\chi}\chi^2 \qquad \textit{Eq. 1-18}$$

Some energies previously cited can cause others to increase or decrease based on the atoms' movement to adjust the bond length or angle change. For example, the bond length between atoms might increase due to a decrease in the bond angle or the opposite. This effect can be incorporated into the potential by the cross terms, which can be decomposed into the interactions of stretching, bending, and torsion and the combination of these terms (Jensen, 2017).

Other interactions may occur for non-bonded atoms due to charge attraction, repulsion, and proximity. The non-bonded energy is often decomposed into the van der Waals and Coulombic terms, as shown in Eq. 1-19.

$$E_{nonbond} = E_{VdW} + E_{Coulomb} \qquad \textit{Eq. 1-19}$$

The van der Waals term describes the interaction energy between atoms that are not directly bonded by incorporating an attraction and repulsion term. For example, this term is mainly associated with a non-polar interaction between two molecules. The van der Waals term is strongly related to the distance between two atoms, as it approaches to zero for large distances and its repulsive component increases at short distances. Due to electron correlation, there is an attractive force between two atoms at some distance, generated by an induced dipole-dipole interaction even for non-polar molecules. A popular representation of van der Waals interactions is the Lennard-Jones potential. The Lennard-Jones potential energy can be represented by the Eq. 1-20, where $\epsilon$is the cohesive energy well depth, σ is the equilibrium distance, and r is the actual distance (Jensen, 2017).

$$E(r)^{LJ} = 4\epsilon\left[\left(\frac{\sigma}{r}\right)^{12} - \left(\frac{\sigma}{r}\right)^{6}\right] \qquad \textit{Eq. 1-20}$$

Along with the van der Waals term, the non-bonded energy is also calculated by the Coulombic interaction between two atoms, also called the electrostatic interaction. This interaction is based on the charges of both particles and can be represented by the Eq. 1-21. In this representation of the Coulombic potential, Q_A and Q_B are the charges in each atom, ε is the dielectric constant and R_{AB} is the distance between the atoms. The simulation input assigns the atomic charges, and the potential equation can assume the form as Eq. 1-22, where $f = \frac{1}{4\pi\varepsilon_0}$ and ε_r is the relative dielectric constant, often assigned the value of 1, considering simulations in vacuum. Although the electrostatic interaction may be represented by other parameters, such as the bond dipole, in the MD simulation input the force field often uses the atomic charge representation.

$$E_{Coulomb} = \frac{Q_A Q_B}{\varepsilon R_{AB}} \qquad \textit{Eq. 1-21}$$

$$E_{Coulomb} = f\frac{Q_A Q_B}{\varepsilon_r R_{AB}} \qquad \textit{Eq. 1-22}$$

To calculate the potential energy from the bonded and non-bonded interactions, a force field is used as a combination of predetermined parameters that will describe the particle interactions (Fehske et al., 2008). Many force fields have been developed to represent sets of molecules with specific parameters. Empirical and simulated data can be used to parameterize the force field, ensuring an accurate representation of quantum mechanical observations and experimental results.

Water was extensively investigated as a common solvent, and many force fields have been developed for this specific molecule. Three-site and four-site force fields have successfully been used to demonstrate the properties of water in MD simulations. The Transferable Intermolecular Potential 4 Points (TIP4P) model is a four-site force field used for

the simulations of water molecules, as shown in Figure 1-3. It incorporates a virtual site for properties correction from previous force fields (Dick and Madura, 2005).

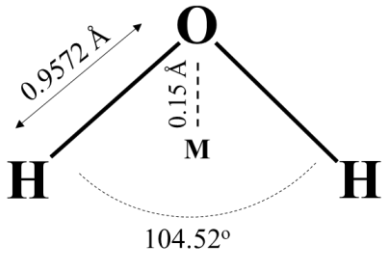

Figure 1-3 TIP4P representation of a water molecule with the virtual site M, OH bond length and HOH angle.

Improvements on the TIP4P model have been developed as Ewald corrections and implemented in the TIP4P-Ew force field. In the TIP4P-Ew model, the values of the parameters are determined based on a combination of experimental values and MD simulated data, and are presented in Table 1-1 and Table 1-2. As the TIP4P force field has a virtual site (M), the force computed by the potential energy is corrected following the equation Eq. 1-23, as it implements the weight w_i for the virtual site (Horn et al., 2004). For the TIP4P-Ew force field, the Lennard-Jones parameters are set as 0.163 kcal.mol-1 for ε and 3.164 Å for σ.

$$\boldsymbol{F}_i = w_i \boldsymbol{F}_s \qquad \textit{Eq. 1-23}$$

Table 1-1 Atomic properties of the TIP4P-Ew force field for the water molecule.

TIP4P-Ew Water

Atom	Charge (e^-)	Mass (*g/mol*)
H	0.524	1.00
O	0.000	16.00
M	-1.048	0.00

Table 1-2 Bond and virtual site parameters for the TIP4P-Ew force field for the water molecule.

TIP4P-Ew Water

Atoms	k_b	b_0 (*nm*)	H_θ	θ (^{o})	*a*	*b*
H-O	502416.0	0.09572	-	-	-	-
H-O-H	-	-	628.02	104.52	-	-
W	-	-	-	-	0.1067	0.1067

Other force fields have been developed to incorporate the parameters for different sets of molecules. The Optimized Potentials for Liquids Simulations – All Atoms (OPLS-AA) force field is designed to include conformational and intermolecular energies for many organic solvents. The OPLS-AA model has been parametrized based on *ab initio* calculations, presenting an improvement relative to the previous OPLS potentials. The OPLS-AA parameters for the cyclohexane molecule are shown in Table 1-3 and

Table **1-4** (Jorgensen et al., 1996).

Table 1-3 Atomic properties of the OPLS-AA force field for the cyclohexane molecule.

OPLS-AA Cyclohexane

Atom	Charge (e^-)	Mass (*g/mol*)	*V* (kJ.mol^{-1}.nm^6)	*W* (kJ.mol^{-1}.nm^{12})
H	0.0870	1.01	0.250	0.126
C	-0.1740	12.01	0.350	0.276

Table 1-4 Bond parameters for the OPLS-AA force field for the cyclohexane molecule.

OPLS-AA Cyclohexane

Atoms	k_b	b_0 (nm)	H_θ	θ (^{o})	C_0	C_1	C_2	C_3
H-C	284512.0	0.1090	-	-	-	-	-	-
C-C	224262.0	0.1529	-	-	-	-	-	-
H-C-C	-	-	313.800	110.7	-	-	-	-
C-C-C	-	-	488.273	112.7	-	-	-	-
H-C-H	-	-	276.144	107.8	-	-	-	-
C-C-C-C	-	-	-	-	2.301	-1.464	0.837	-1.674
H-C-C-C	-	-	-	-	0.628	1.883	0	-2.510

As described previously, in calculating all potential and kinetic energy, the simulation follows the derivative of the potential energy with respect to the particle position, as shown in Eq. 1-6. By following the equation of motion, the energy derivative can be translated to the force applied to the particle, and consequently, the acceleration may be calculated. For a set of particle positions r_i, the change in position after a time step Δt can be expressed by a Taylor series expansion, as represented by Eq. 1-24 (Rapaport, 2004).

$$\boldsymbol{r}(t+\Delta t) = \boldsymbol{r}(t) + \Delta t * \frac{\partial \boldsymbol{r}}{\partial t} + \frac{1}{2}\Delta t^2 * \frac{\partial^2 \boldsymbol{r}}{\partial t^2} + \cdots \qquad \textit{Eq. 1-24}$$

The second and third terms of the expansion of the particle motion have derivatives equal to the velocity ($\boldsymbol{v}$) and acceleration ($\boldsymbol{a}$), respectively. Replacing the velocity and acceleration in Eq. 1-24, it is possible to represent the motion by Eq. 1-25. A similar representation can be made by determining a step back and subtracting a time step Δt, as shown

in Eq. 1-26. Eq. 1-26 can be added to the Eq. 1-25 to calculate the velocity, as expressed by Eq. 1-27. This calculation is known as the Verlet algorithm (Grubmüller et al., 1991).

$$\boldsymbol{r}(t+\Delta t) = \boldsymbol{r}(t) + \Delta t * \boldsymbol{v}(t) + \frac{1}{2}\Delta t^2 * \boldsymbol{a}(t) \qquad \textit{Eq. 1-25}$$

$$\boldsymbol{r}(t-\Delta t) = \boldsymbol{r}(t) - \Delta t * \boldsymbol{v}(t) + \frac{1}{2}\Delta t^2 * \boldsymbol{a}(t) \qquad \textit{Eq. 1-26}$$

$$\boldsymbol{r}(t+\Delta t) + \boldsymbol{r}(t-\Delta t) = 2\boldsymbol{r}(t) + \Delta t^2 * \boldsymbol{a}(t)$$

$$\boldsymbol{r}(t+\Delta t) = 2\boldsymbol{r}(t) - \boldsymbol{r}(t-\Delta t) + \Delta t^2 * \boldsymbol{a}(t) \qquad \textit{Eq. 1-27}$$

The Verlet algorithm is widely used as a numerical method to determine particles' acceleration, velocity, and position. Based on Eq. 1-6, following the calculation of the potential energy and the force on the particles, the acceleration is determined and inserted in Eq. 1-27 to calculate the velocity and new position. The algorithm is based on the repetition of this calculation during a pre-established time *t* (Rapaport, 2004). The Verlet algorithm may lead to a truncation error since it has in its equation the Δt^2, which will result in a very small number multiplied by $(2r(t) - r(t - \Delta t))$. For a numerical correction and the lack of explicit velocity on the expressions presented by the Verlet algorithm, the Velocity Verlet algorithm was proposed to cover these deficiencies. The Velocity Verlet algorithm starts with the Taylor series expansion of position, shown in Eq. 1-25, and the velocity equation is described in Eq. 1-28. The steps followed by this algorithm establish the calculation of the velocity at a time step $\Delta t/2$, followed by the calculation of the position after the time step Δt. By acquiring the acceleration from the energy and force calculation, the velocity after a time step Δt can be calculated, and the algorithm can repeat itself. All the equations related to the Velocity Verlet algorithm can be seen, leading to Eq. 1-29 (Fehske et al., 2008).

$$\boldsymbol{v}(t+\Delta t) = \boldsymbol{v}(t) + \frac{1}{2}\Delta t * [\boldsymbol{a}(t) + \boldsymbol{a}(t+\Delta t)] \qquad \textit{Eq. 1-28}$$

$$\boldsymbol{v}\left(t+\frac{\Delta t}{2}\right) = \boldsymbol{v}(t) + \frac{1}{2}\Delta t * \boldsymbol{a}(t)$$

$$\boldsymbol{r}(t+\Delta t) = \boldsymbol{r}(t) + \Delta t * \boldsymbol{v}\left(t+\frac{\Delta t}{2}\right)$$

$$\boldsymbol{v}(t+\Delta t) = \boldsymbol{v}\left(t+\frac{\Delta t}{2}\right) + \frac{1}{2}\Delta t * \boldsymbol{a}(t+\Delta t) \qquad \textit{Eq. 1-29}$$

By correctly applying the Verlet algorithm or its modification to the Velocity Verlet algorithm, the system's energy will be conserved within the method's accuracy. Figure 3 illustrates the start of the simulation and the algorithm to obtain the next steps. This process leads the MD simulation to apply a microcanonical ensemble (NVE), where the number of molecules in the unit cell is constant (N), the volume of the unit cell is also not changing (V), and the energy is conserved by the algorithm (E). However, many experimental procedures simulated by the MD method need a temperature or pressure control. These restrictions to the system result in different ensembles, such as the canonical ensemble (NVT) and the isobaric-isothermal (NPT). Those ensembles are established by controlling the temperature with a thermostat and the pressure with a barostat (Lemak and Balabaev, 1994).

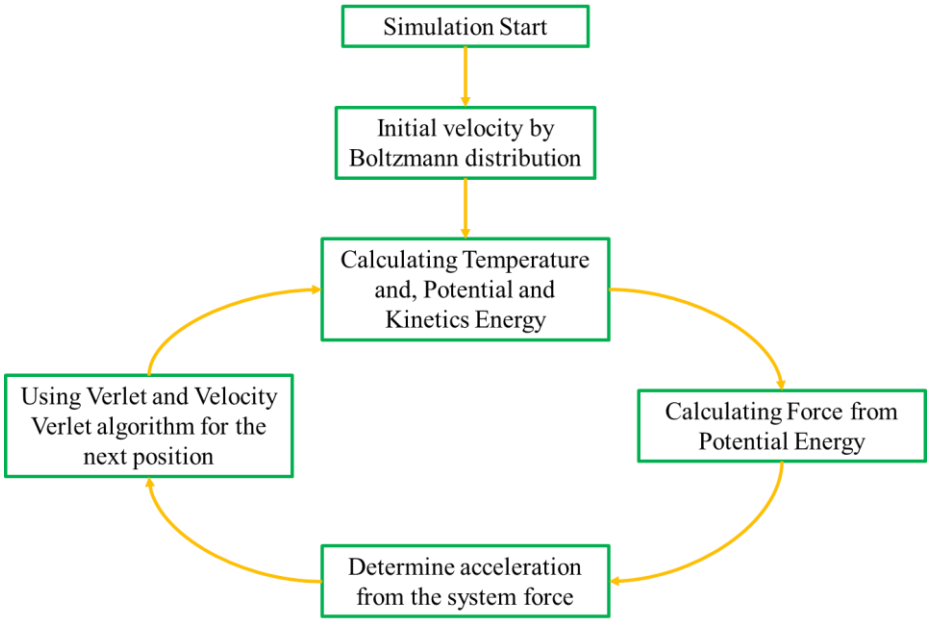

Figure 1-4 Flow chart for the simulation start and determination of new positions.

The thermostat applied in MD simulations can be associated with a heat bath. The simplest thermostat can be used by simply scaling the velocities to influence the system's temperature to the desired temperature. However, this method may cause large fluctuations in the total energy. To overcome this issue, several thermostats aim to reproduce the ensembles and accurately control the temperature. The Berendsen thermostat slowly corrects the temperature and suppresses the kinetic energy oscillations. This thermostat operates with a temperature set for the system T_0 and a dumping factor τ. The change in the temperature (T) can be determined by Eq. 1-30, using the dumping factor to determine the control strength of the thermostat and can be adjusted by the user (Van Gunsteren and Berendsen, 1990).

$$\frac{dT}{dt} = \frac{T_0 - T}{\tau} \qquad Eq.\ 1\text{-}30$$

The temperature coupling is introduced by adjusting the velocities by a time-dependent factor λ, as depicted in Eq. 1-31. It is used for every temperature coupling step, n_{TC},by applying a parameter τ_T, shown in Eq. 1-32.

$$\lambda = \sqrt{1 + \frac{n_{TC}\Delta t}{\tau_T}\left(\frac{T_0}{T\left(t - \frac{1}{2}\Delta t\right)} - 1\right)} \qquad \textit{Eq. 1-31}$$

$$\tau = \frac{2C_V\tau_T}{N_{df}k} \qquad \textit{Eq. 1-32}$$

In Eq. 1-32, C_v is the heat capacity, N_{df} is the number of degrees of freedom, and k is the Boltzmann's constant. The Berendsen thermostat influences the velocity by modifying the kinetic energy according to Eq. 1-33.

$$\Delta E_{kin} = (\lambda - 1)^2 E_{kin} \qquad \textit{Eq. 1-33}$$

The kinetic energy correction is also approached by another thermostat, called Velocity Rescaling. The expression for this thermostat adds a new term on the correction of the kinetic energy and can be seen in Eq. 1-34. For the velocity-rescaling thermostat, the kinetic energy correction includes the Wiener process (W) (Bussi et al., 2009).

$$dE = \left(E_{kin,0} - E_{kin}\right)\frac{dt}{\tau_T} + 2\sqrt{\frac{E_{kin} * E_{kin,0}}{N_{df}}} * \frac{dW}{\sqrt{\tau_T}} \qquad \textit{Eq. 1-34}$$

Similarly, to ensure an isobaric condition on the NPT ensemble, some simulations can use a barostat to enforce constant pressure on the system. The pressure P can be calculated by applying the kinetic energy and the virial term, both represented by Eq. 1-35 (Parrinello and Rahman, 1981).

$$P(r,t) = \frac{2}{V}\left[\sum_{i=1}^{N} m_i \boldsymbol{v}_i^2(t) + \sum_{i=1}^{N}\sum_{j>1}^{N} \boldsymbol{r}_{ij}(t)\boldsymbol{F}_{ij}(t)|_{r_i(t)=r}\right] \qquad \textit{Eq. 1-35}$$

Several algorithms used in MD software can support an isobaric simulation, such as the Parrinello-Rahman barostat. Using a matrix to incorporate the system vectors ($\boldsymbol{b}$), the Parrinello-Rahman approach represents the equation of motion, as shown in Eq. 1-36, where V represents the volume, **W** is the matrix parameter that determines the coupling strength, P

refer to the pressure, and P_{ref} is the reference pressure. The inverse matrix W^{-1} determines how strong the coupling will be and how the box can deform during the simulation. The inverse of the matrix can be represented by the Eq. 1-37, where it incorporates the parameter τ_P as the pressure time constant, the isothermal compressibility β, and the largest box matrix element $\boldsymbol{L}$.

$$\frac{d\boldsymbol{b}^2}{dt^2} = V\boldsymbol{W}^{-1}\boldsymbol{b}'^{-1}\left(P - P_{ref}\right) \qquad \textit{Eq. 1-36}$$

$$(\boldsymbol{W}^{-1})_{ij} = \frac{4\pi^2\beta_{ij}}{3\tau_P^2\boldsymbol{L}} \qquad \textit{Eq. 1-37}$$

Although establishing an ensemble for the simulation and reaching an equilibrium for the energy in determining temperature and pressure conditions are crucial to the simulation, the first step required for an MD simulation is taken by energy minimization. The energy minimization step investigates the Potential Energy Surface (PES) for the lowest energy that a structure or a system can assume. In the MD method, this step can be done using several approaches, such as the steepest decent (SD) and conjugate gradient algorithm (Gautam, 2021). The SD minimization is a first derivative method, as it uses a normalized gradient vector to establish the direction in which the particle will be displaced for minimal energy. Eq. 1-38 shows how the new position for a particle ($\boldsymbol{r}_n$) is determined for each step n , using the forces determined by the potential energy and its maximum scalar value. The force is divided by its maximum value $max(|\boldsymbol{F}_n|)$ and multiplied by the step size factor h_n; this term is then added to the current position ($\boldsymbol{r}_n$). After determining the direction, the size of the step the particle needs to take can be established by applying a default factor. By this approach, the particle will be placed in another configuration, where, if the potential energy is lower, the factor can be increased, and if it is greater than the previous step, the last step will be repeated and submitted to a smaller step size. These steps are illustrated in Eq. 1-39.

$$\boldsymbol{r}_{n+1} = \boldsymbol{r}_n + \frac{\boldsymbol{F}_n}{max(|\boldsymbol{F}_n|)} h_n \qquad \textit{Eq. 1-38}$$

$$If\ (E_{pot})_{n+1} < (E_{pot})_n \rightarrow h_{n+1} = 1.2h_n$$

$$If\ (E_{pot})_{n+1} \geq (E_{pot})_n \rightarrow h_n = 0.2h_n \qquad \textit{Eq. 1-39}$$

In summary, the MD simulation undergoes several steps before it can be analyzed for any property for a specific objective, as shown in Figure 1-5. The first step starts with the system construction and the selection of a force field. Here, the force field contains all parameters used for calculating the bonded and non-bonded potential energy of the chosen molecular system. After establishing the unit cell size and inserting the molecules, the energy minimization step discussed previously is conducted, followed by an equilibration step. The equilibration step can involve different ensembles used in simulations to ensure that the system configuration meets the specific conditions. For example, it is common to perform a simulation using the canonical ensemble (NVT) before conducting an isobaric-isothermal (NPT) simulation. This method helps the system establish an equilibrium within the simulation time.

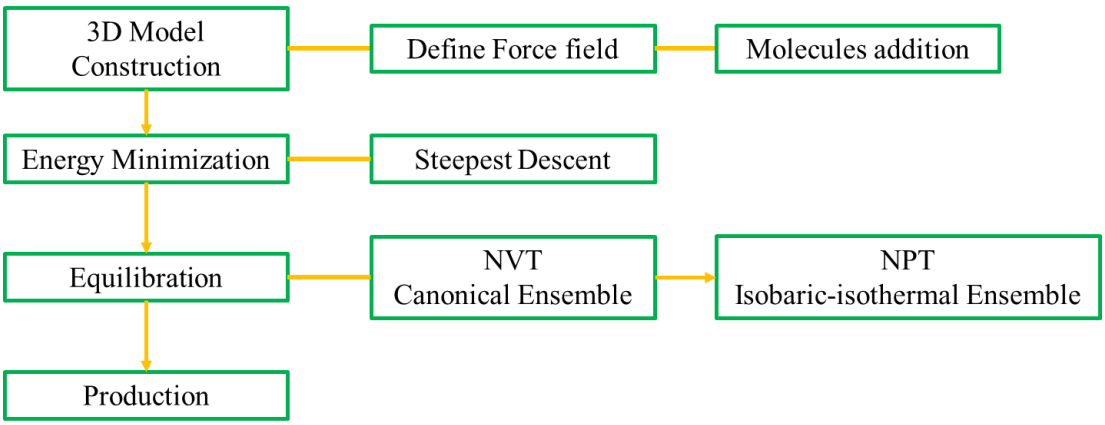

Figure 1-5 Flow chart to illustrate the molecular dynamics simulations until the production phase.

After achieving an equilibrium, the simulation can be performed to extract the desired data and undergo any condition that can disturb the equilibrium, e.g., an electric field (*E*). In various MD software, it is possible to apply an electric field on the unit cell, which will influence the final force computed for the equation of motion as represented by Eq. 1-40. This equation describes the electric field, *E(t)*, and the magnetic field, *B(t)*, that are present in microwave heating, with the electric field being multiplied by the charge (q_i) on each particle and the magnetic field by the charge and velocity (v_i) of the particle *i* (Chen et al., 2023). The overall force after the electric field application is used on the Eq. 1-5 to determine the particles' acceleration.

$$\boldsymbol{F}_{Total} = \boldsymbol{F}_i + q_i\boldsymbol{E}(t) + q_i\boldsymbol{v}_i \times \boldsymbol{B}(t) \qquad \textit{Eq. 1-40}$$

Although experimentally the magnetic field is acting on samples, the intensity of a magnetic field is considerably smaller than the electric field by the relation in Eq. 1-41, where the amplitude of the magnetic field (B_0) is equal to the amplitude of the electric field (E_0) over the speed of light (*c*). This justifies the use of only an electric field to determine a microwave heating through MD simulations (Chen et al., 2023).

$$B_0 = \frac{1}{c} * E_0 \qquad \textit{Eq. 1-41}$$

The electric field applied in the MD simulation can be described by Eq. 1-42, incorporating the electric field strength, E_0, and the angular frequency, ω. It is widely reported that the electric field strength for an MD simulation is increased to provide an observable temperature change in the time frame used in this method. In the literature, the electric field strength is often set from 0.01 to 1 V/nm, considerably higher than that used in household and industrial microwaves (English and Waldron, 2015). The literature also mentions using a higher frequency to promote the rotational movement of dipoles, where many research papers

apply the frequency of 100 GHz, which is higher than 2.45 GHz and 915 MHz commonly found in experimental procedures for microwave heating.

$$\boldsymbol{E}(t) = E_0 cos(\omega t) \qquad \textit{Eq. 1-42}$$

Although most MD simulations use thermodynamic ensembles in equilibrium, the application of electric field on a unit cell will result in a non-equilibrium molecular dynamics (NEMD) simulation. The non-equilibrium condition generated by an electric field is described in the literature, by English *et al.*, by simulating the microwave heating with different ensembles (English and MacElroy, 2003a). The authors explore the electric field influence on the water molecules, establishing a non-equilibrium Newtonian ensemble (NNMD) and a non-equilibrium canonical ensemble (NNPT). Both ensembles were used to determine different properties of molecular diffusion. However, the literature lacks calculations using a barostat without a thermostat, as this would allow a temperature variation after the electric field application, keeping experimental conditions, e.g., atmospheric pressure. The absence of pressure and temperature controls, as in the NNMD simulation, can be an alternative to explore the electric field heating in a confined space, since it would have a constant volume condition and a local increase in pressure and temperature.

As mentioned in Section 1.2, the electric field greatly influences the rotation of the molecule's dipole. The rotation promotes molecular motion, increasing the temperature since temperature is a function of the motion of molecules (translational, rotational and vibrational). The rotational autocorrelation function (RAF) is one parameter that can be analyzed to determine the electric field's influence on the rotational motion of molecules. A rotational autocorrelation function for each time step is the scalar product of the initial position vector and the position at the time *t* averaged for all molecules (Guo et al., 2020). The literature describes the square function as a cosine function, as shown in Eq. 1-43.

$$C_R^2(t) = (1/2) * \langle 3\cos^2\theta\,(t) + 1 \rangle \qquad \text{Eq. 1-43}$$

The rotation autocorrelation function decorrelates from 1 (initial state) to 0 (final state) and indicates how long it takes for the decorrelation of the rotational motion to occur, where θ is the rotational angle from the molecule's rotational motion (Shi et al., 2023). In general, the decorrelation process would take about 100 ps or less to complete.

In addition to the molecular rotation, the temperature change caused by the translational motion can be determined by its diffusion coefficient (*D*). The diffusion coefficient can be calculated by the Einstein relation described in Eq. 1-44, where *T* is the system temperature, k_B is the Boltzmann constant, and μ is the particle mobility (Allen and Tildesley, 2017).

$$D = \mu k_B T \qquad \text{Eq. 1-44}$$

In MD simulations, the diffusion coefficient is determined by the mean square displacement (MSD), which can be calculated by the change in the particle's position in comparison to its initial configuration. The Eq. 1-45 expresses the MSD calculation performed by statistical mechanics, where N is the number of particles to be averaged. The diffusion coefficient, defined as the slope extracted from the linear fitting of the MSD calculation over the simulation time *t*, has been reported in literature to describe the translational motion of molecules under an electric field (English, 2006).

$$MSD \equiv \frac{1}{N}\sum_{i=1}^{N} |\boldsymbol{r}_i(t) - \boldsymbol{r}_i(0)|^2 \qquad \text{Eq. 1-45}$$

1.4 Objective and Scope of the Project

After NAE, the oil sands gangue material can contain water and cyclohexane in close proximity or in the same pore. This study aims at improving our understanding of microwave heating and its mechanism that allows cyclohexane recovery from the microwave heating process, as presented in Figure 1-1. A challenge that arises from the experimental procedure is

the limitation to confirm the mechanism by which the cyclohexane can be heated by the MWH, as cyclohexane molecules are considered transparent to microwaves. This is because the cyclohexane molecule has no permanent dipole moment. It is expected that water molecules absorb the power introduced by the MWH and transfer the energy to nearby cyclohexane molecules through molecular motion.

The objective of this study is to explore and explain the mechanism of heating of fluid systems containing water and cyclohexane using external electric field applications, which simulate microwave heating. The energy transfer will be observed by the time evolution of temperature and comparing the behaviors of monophasic and biphasic systems. The monophasic analysis has the objective of ensuring the methodology can reproduce the heating of water molecules and the transparency of cyclohexane to the electric field. The simulated biphasic system aims to reproduce the mixture found in the wet gangue from the solvent extraction of bitumen and to investigate the heating mechanism between water and cyclohexane from an electric field heating.

The scope of the study includes the simulation of 2 liquids, water and cyclohexane, in mono- and biphasic systems. The study limits the electric field to a single plan (xy) wave applied through the z-axis of a rectangular unit cell and does not account for any interfacial interaction. The applied electric field consists of 3 different frequencies, to simulate the industrial and domestic microwave frequencies (915 MHz and 2.45 GHz, respectively) and the frequency of 100 GHz to potentialize the electric field action in the aforementioned molecules. Additionally, the electric field is applied using the electric field strengths of 0.01 V/nm and 3 V/nm to analyze the influence of the field intensity on the heating mechanism. To perform the temperature analysis, the project has as its scope the use of MD simulations to reproduce pure water and cyclohexane systems as well as their biphasic mixture. Since the MD method is used

in nanometer and nanosecond scales, the study aims for a qualitative analysis rather than ensuring a precise temperature increase or energy transferred from water to cyclohexane.

2 Molecular Dynamics Simulation Methodology

The MD simulations were performed using the software GROMACS (Van Der Spoel *et al*., 2005). Such simulations generally start with constructing a unit cell containing molecules of interest, followed by energy minimization and equilibration. The energy minimization step is used to ensure the stability of the subsequent MD simulation. The production runs were carried out with and without the electric field imposed on the unit cell. To describe the interatomic interactions, the TIP4P-Ew potential was used for water molecules, and the OPLS-AA potential was applied to cyclohexane molecules. The cyclohexane topology parameters are obtained from the LIGPARGEN web server (Dodda *et al*., 2017b, 2017a; Jorgensen and Tirado-Rives, 2005).

2.1 Unit cells construction

The MD simulations were carried out using a rectangular prism-shaped unit cell, as illustrated in Figure 2-1. This nanometric prism has equal sides on the square base (x and y axes). For monophasic systems, the unit cells were constructed with the dimensions of 5 × 5 × 5 nm^3. For the biphasic systems, the simulation cells were initially built with dimensions of 4.5 × 4.5 × 7 nm^3, where the water layer is placed underneath the cyclohexane layer. The cyclohexane layer has a dimension of 4.5 × 4.5 × 4.5 nm^3. As a result, the water layer has a thickness of 2.5 nm. Such a biphasic simulation unit cell is shown in Figure 2-2.

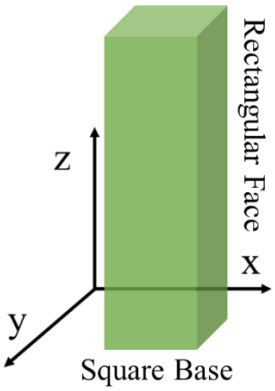

Figure 2-1 Representation of a right square prism unit cell with Cartesian coordinates. The size of the square-base is fixed while the height of the unit cell on the *z*-axis varies.

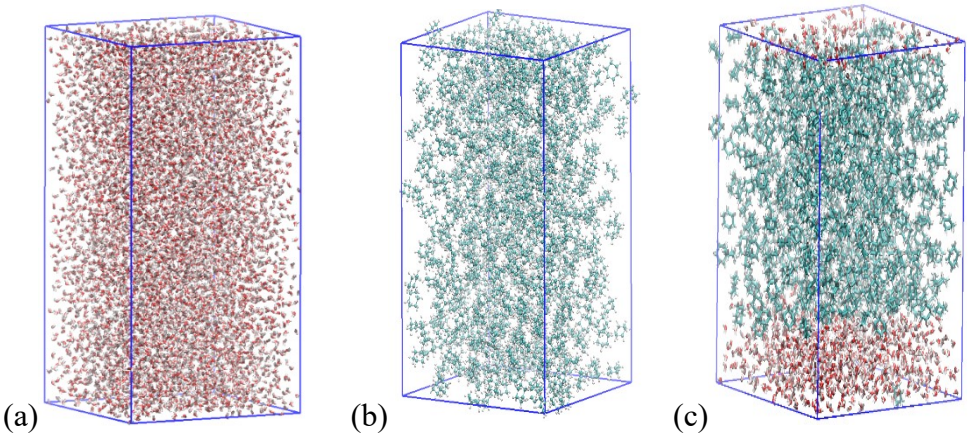

Figure 2-2 A unit cell of (a) water monophasic and (b) cyclohexane monophasic system, and (c) biphasic system with a bottom layer of water molecules (oxygen atoms in red and hydrogen atoms in light grey) and an upper layer of cyclohexane (carbon atoms in green and hydrogen atoms in light grey) in the unit cell.

2.2 Simulations details

Several steps were undertaken to simulate all the mono- and biphasic unit cells before applying an electric field through the unit cell. The energy minimization was done using the steepest descent method, with a threshold of 10 $kJ \cdot mol^{-1} \cdot nm^{-1}$. The next step was equilibration, and it was carried out using the canonical ensemble (NVT) for 10 ns, using the canonical

ensemble (i.e., constant number of molecules in the unit cell, N, constant volume, V, and constant temperature, T). The constant volume was assured by the absence of a barostat and for the constant temperature aspect, the V-rescale thermostat was used to regulate the temperature of the system, with a damping factor of 1.0 ps and the temperature was set to 298 K. After the NVT MD annealing, isobaric and isothermal ensemble (NPT) MD simulations were performed for 10 ns allowing volume change volume, thereby reaching the condition of 1 bar and 300 K. The thermostat used in the NPT MD annealing was the same as that used for the NVT annealing and the pressure was controlled by the Parrinello-Rahman barostat with a damping factor of 2.0 ps to ensure that the pressure of the calculation was kept constant. These equilibration steps were adopted following similar procedures presented in the literature (Shi *et al*., 2023).

After the unit cell equilibration, the MD simulations were conducted for 10 ns under non-equilibrium conditions. The simulations were set up without a thermostat, and two approaches were conducted: with the barostat set at one bar and simulations without a barostat with a constant volume of ~150 nm^3 to ensure a constant density of the system. Simulations with and without the external field were performed to establish the temperature increase caused by the electric field. The temperature values signify the difference between both simulations and the initial temperature of 27ºC (300 K).

In the simulations, the electric field was applied perpendicular to the unit cell's square base (see Figure 2-1) with strength set for 0.01 V/nm and 3.00 V/nm. The frequency for the simulations was set to 915 MHz, 2.45 GHz, and 100 GHz. The highest frequency was evaluated due to its presence in literature and its elevated influence on the rotation of dipoles. The electric field illustration is shown in Figure 2-3. The simulation protocol, shown in Figure 2-4, presents the steps for producing the MD trajectories under an electric field.

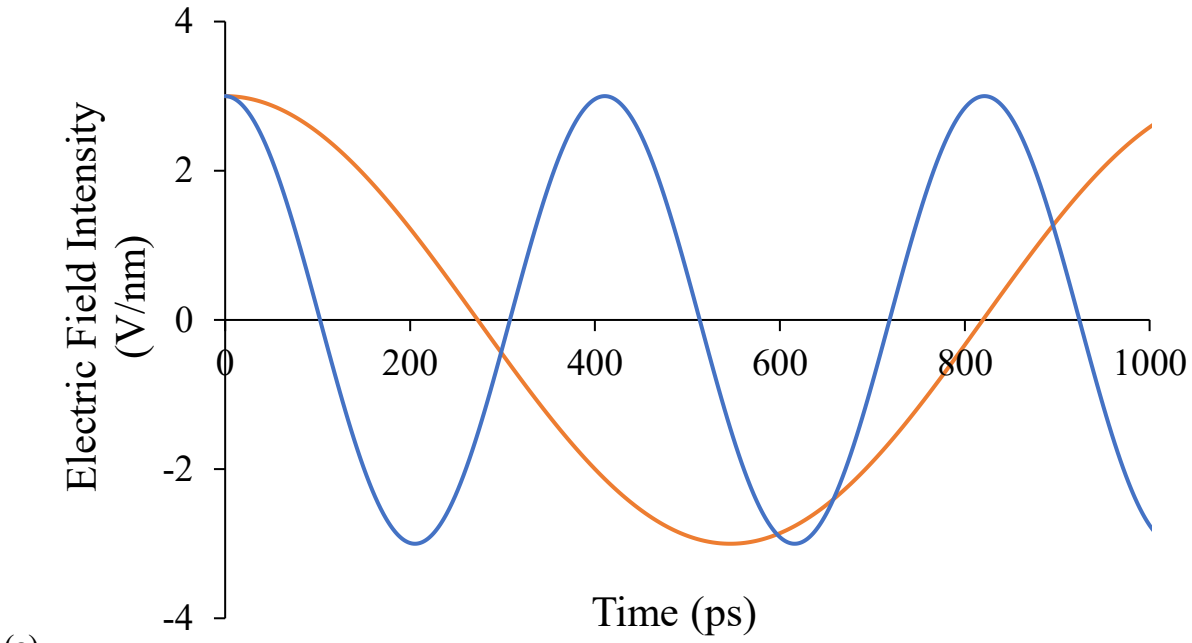

(a)

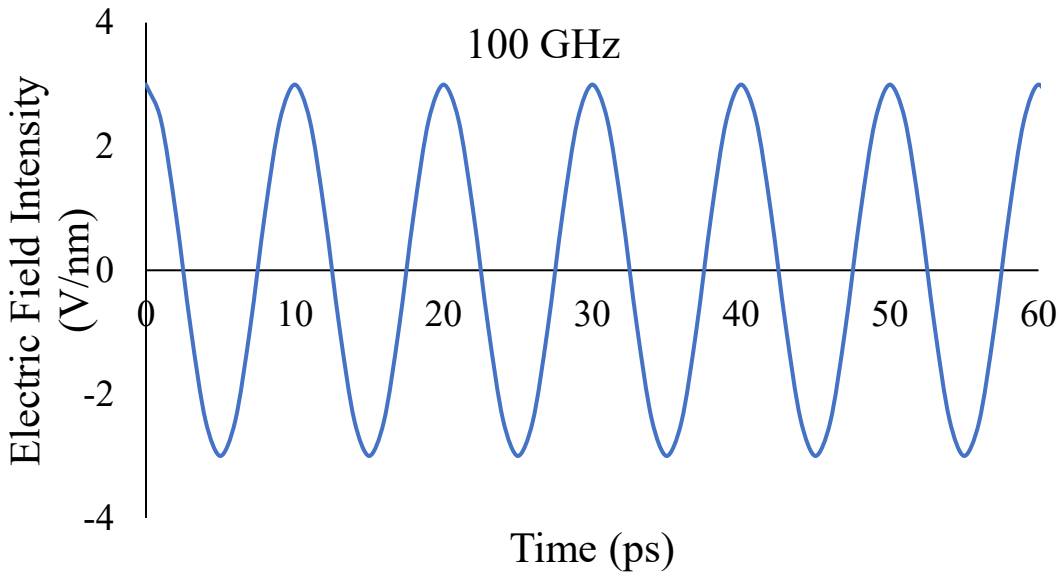

(b)

Figure 2-3 Illustration of the electric field applied in the molecular dynamics simulations for frequencies of (a) 915 MHz (orange) and 2.45 GHz (blue) and (b) for 100 GHz.

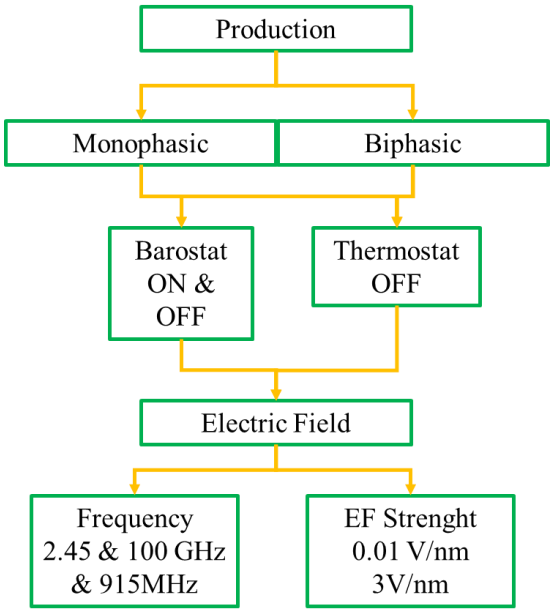

Figure 2-4 The MD simulation protocol for MD simulation of monophasic and biphasic systems under an electric field.

3 Results and Discussion

The MD simulations were performed with and without applying the electric field to the monophasic and biphasic systems. For the monophasic systems, the MD simulations were performed to analyze the responses of pure water and pure cyclohexane to the applied electric field and the associated temperature changes. The biphasic system simulations were performed to investigate the temperature changes and mechanism of microwave heating of the two immiscible liquids.

3.1 Monophasic Systems – Water and Cyclohexane

The simulations were conducted in the conditions of constant pressure and constant volume for the monophasic analysis of water and cyclohexane. Those are performed without applying the thermostat for the same unit cells. The RAF was taken to investigate the influence of the imposed electric field on the rotational motion of molecules.

3.1.1 *Constant Pressure Simulations*

Having a permanent dipole, water molecules exhibit a high sensitivity to the oscillating electric field. The microwave heating of water, as shown in literature, has been simulated using MD simulations (English, 2006; English and MacElroy, 2003b; Shi *et al*., 2023). As mentioned in section 1.3, a higher electric field strength needs to be applied in MD simulations to yield an observable heating effect, which manifests in a temperature increase rate comparable to experimental measurements. For example, by applying an electric field with a strength of 0.01 V/nm and frequency of 2.45 GHz, pure water underwent a slow temperature increase over 10 ns of MD simulation. The temperature increase was linear and the final temperature increased by 7^{o}C higher, as shown in Figure 3-1.

The MD simulation performed for pure cyclohexane under the same conditions as for pure water yielded no temperature increase, as shown in Figure 3-2. In Figure 3-3, the two monophasic systems were compared, with water in blue and cyclohexane in orange line colors. The electric field applied for both simulations was sufficiently strong to provide a slight but clear distinction between the behaviors of these liquids.

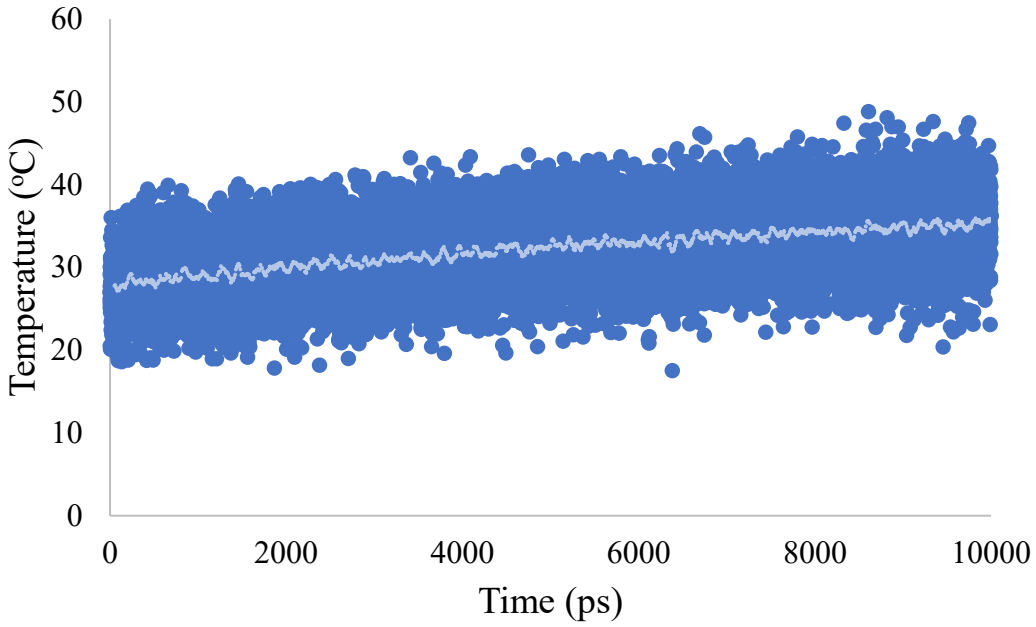

Figure 3-1 Time evolution of the temperature of water in a monophasic system subjected to an electric field of 0.01 V/nm and 2.45 GHz at a constant pressure of 1 bar. The moving averages of the two systems are shown in corresponding lighter colours.

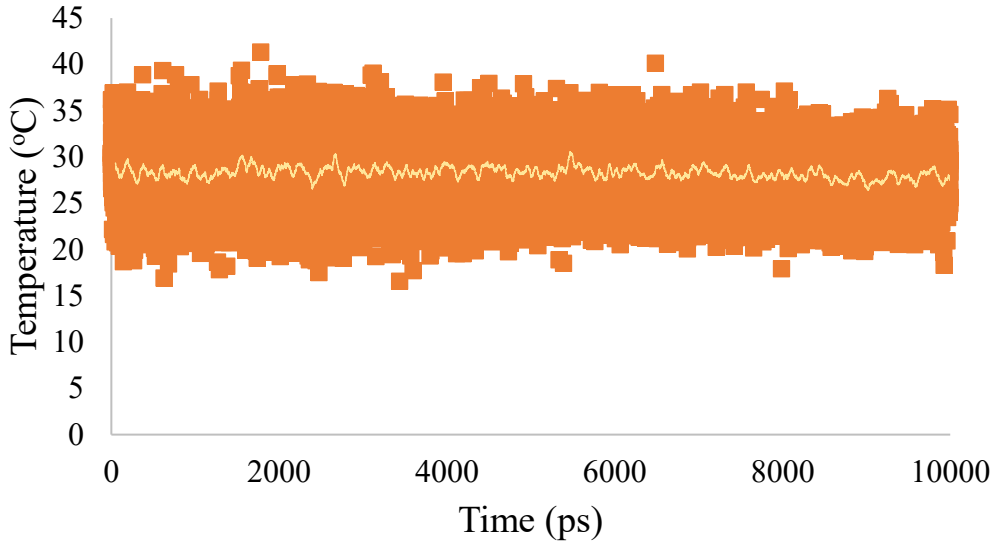

Figure 3-2 Time evolution of the temperature of cyclohexane in a monophasic system subjected to an electric field of 0.01 V/nm and 2.45 GHz at a constant pressure of 1 bar. The moving averages of the two systems are shown in corresponding lighter colours.

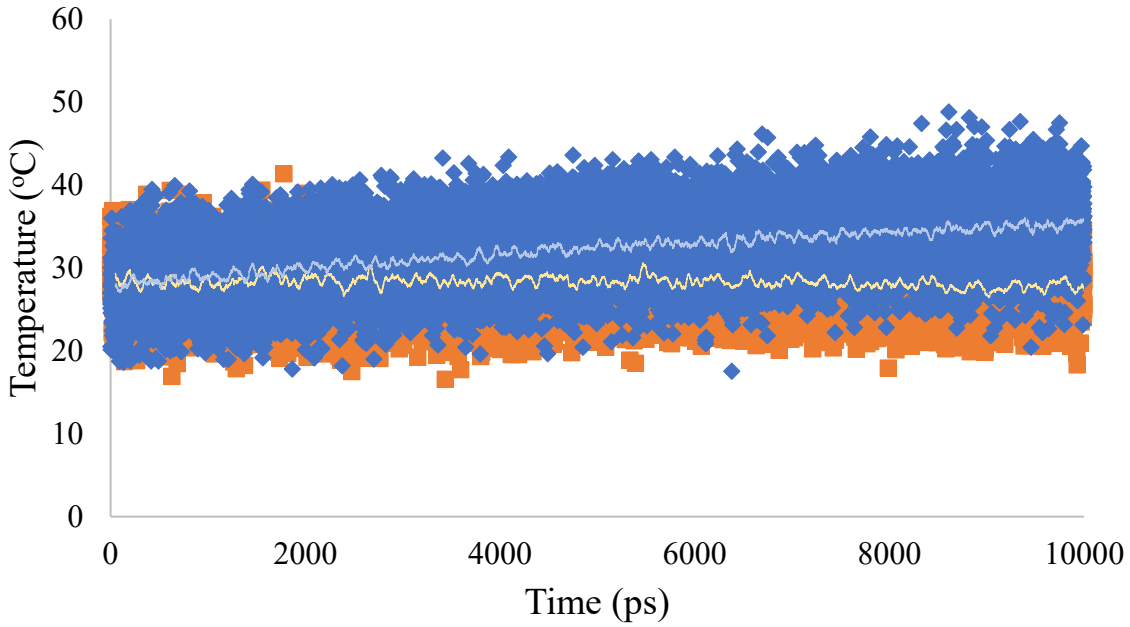

Figure 3-3 Comparison between the temperature evolutions of water (blue) and cyclohexane (orange) in respective monophasic systems subjected to an electric field of 0.01 V/nm and 2.45 GHz at a constant pressure 1 bar. The moving averages of the two systems are shown in corresponding lighter colours.

The above results clearly show that cyclohexane is transparent to microwave, while water absorbs the microwave energy. To test if a much higher microwave frequency would yield a similar observation, 100 GHz was used. In the molecular simulation literature, 100 GHz has been reported to significantly increase water molecules' rotational motion (English and MacElroy, 2003b). In these simulations, pure water exhibits a temperature increase considerably higher than that shown in Figure 3-1. Although the same simulation time (i.e., 10 ns) was used in the 100 GHz simulations, the MD simulation of water was not completed, as the temperature increase exceeded 3000°C. Therefore, Figure 3-4 and Figure 3-5 only report the data up to 1 ns for water and cyclohexane, respectively. Nonetheless, the high frequency results corroborate the low frequency observation shown in Figure 3-3.

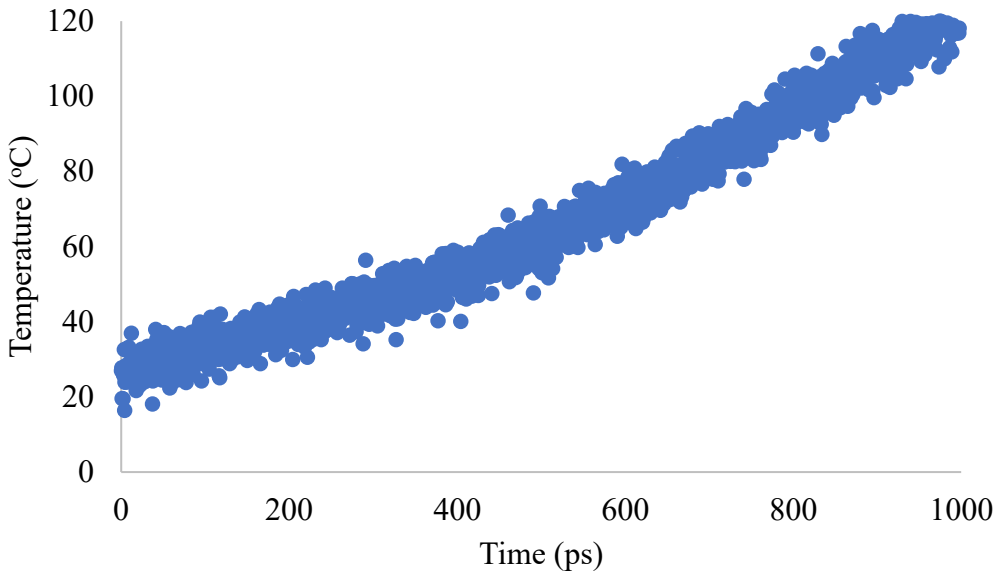

Figure 3-4 Time evolution of the temperature of water in a monophasic system subjected to an electric field of 0.01 V/nm and 100 GHz at a constant pressure of 1 bar.

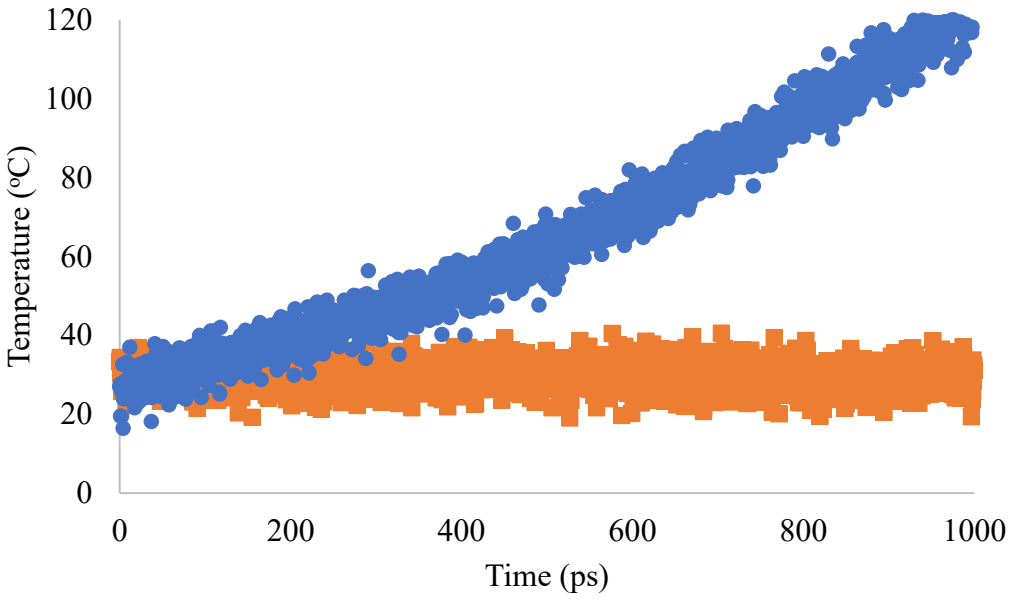

Figure 3-5 Comparison between the temperature evolutions of water (blue) and cyclohexane (orange) in respective monophasic systems subjected to an electric field of 0.01 V/nm and 100 GHz at a constant pressure of 1 bar.

The effect of the electric field strength was also studied at two different frequencies. In particular, MD simulations with the electric field strength (E_0) of 3 V/nm and frequencies of 915 MHz and 2.45 GHz were conducted for 200 ps. Figure 3-6 depicts the simulation result using 3 V/nm and a frequency of 915 MHz, a frequency commonly used industrially. A rapid increase in the temperature for water is noticeable, reaching a maximum temperature of around 200°C almost instantly. The temperature slowly decreases until the end of the simulation, which differs from the pure water behaviour, when a frequency of 2.45 GHz was used, as shown in Figure 3-7. However, when 2.45 GHz was used, water shows a quicker temperature decrease after reaching 200°C. The temperature decrease stops at around 110 ps, and then the temperature increases again.

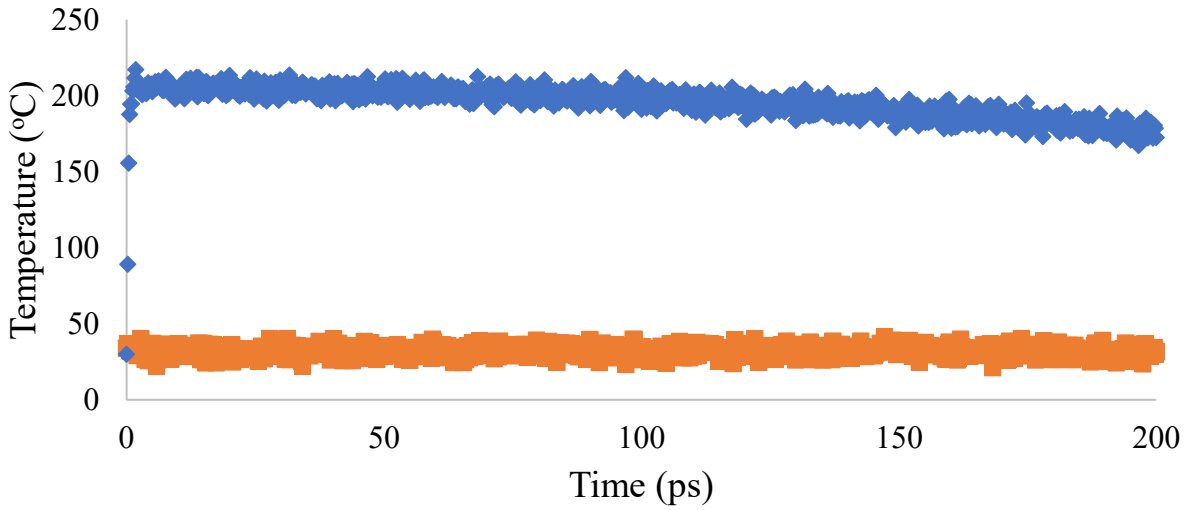

Figure 3-6 Comparison between the temperature evolutions of water (blue) and cyclohexane (orange) in respective monophasic systems subjected to an electric field of 3.0 V/nm and 915 MHz at a constant pressure of 1 bar.

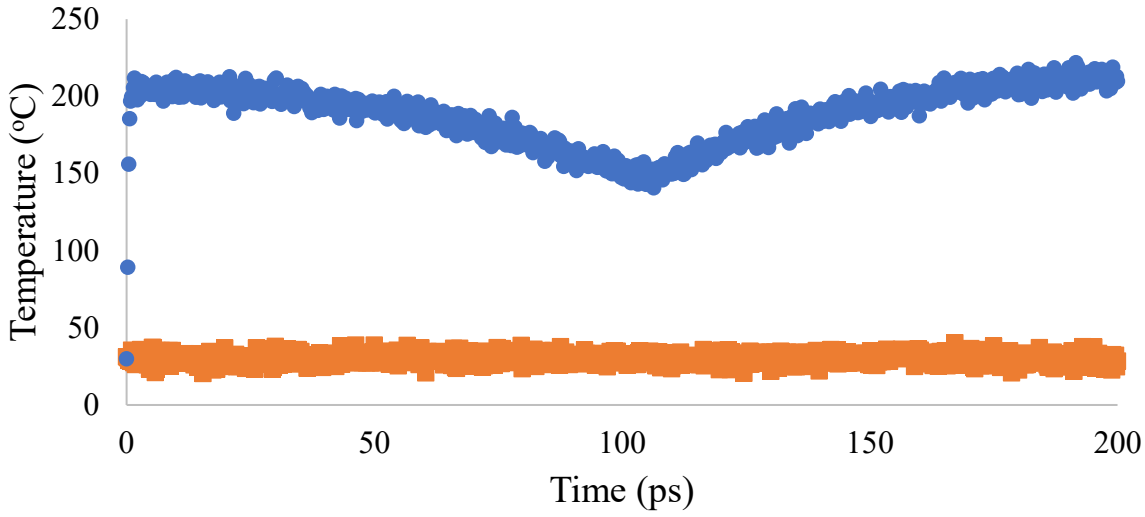

Figure 3-7 Comparison between the temperature evolutions of water (blue) and cyclohexane (orange) in respective monophasic systems subjected to an electric field of 3.0 V/nm and 2.45 GHz at a constant pressure of 1 bar.

The reason for the temperature decrease (Figure 3-6) and the decrease followed by an increase (Figure 3-7) for water can be elucidated by simulations developed for a more extended period. Figure 3-8 and Figure 3-9 show the temperature evolution for 1 ns and present more oscillations for the frequencies of 915 MHz and 2.45 GHz. These figures are also associated with the electric field function (see Figure 2-3), where it is possible to observe the correlation between the electric field intensity and water temperature. The minima of the temperature match the times of zero intensity of the applied electric field.

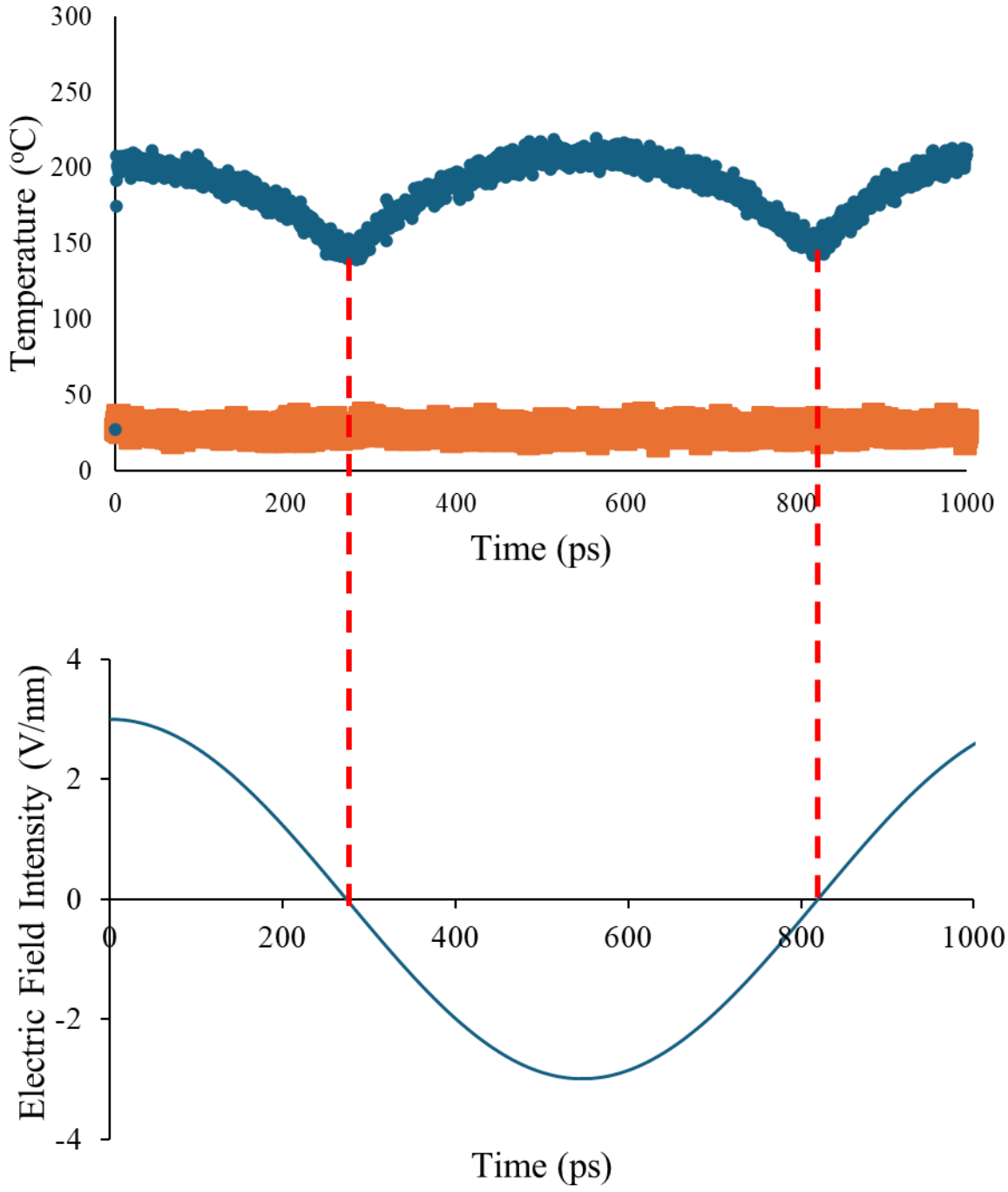

Figure 3-8 Temperature evolution for water (blue) and cyclohexane (orange) in respective monophasic system for 1 ns and the corresponding electric field wave at 915 MHz. Dashed red lines represent the same time for both graphs.

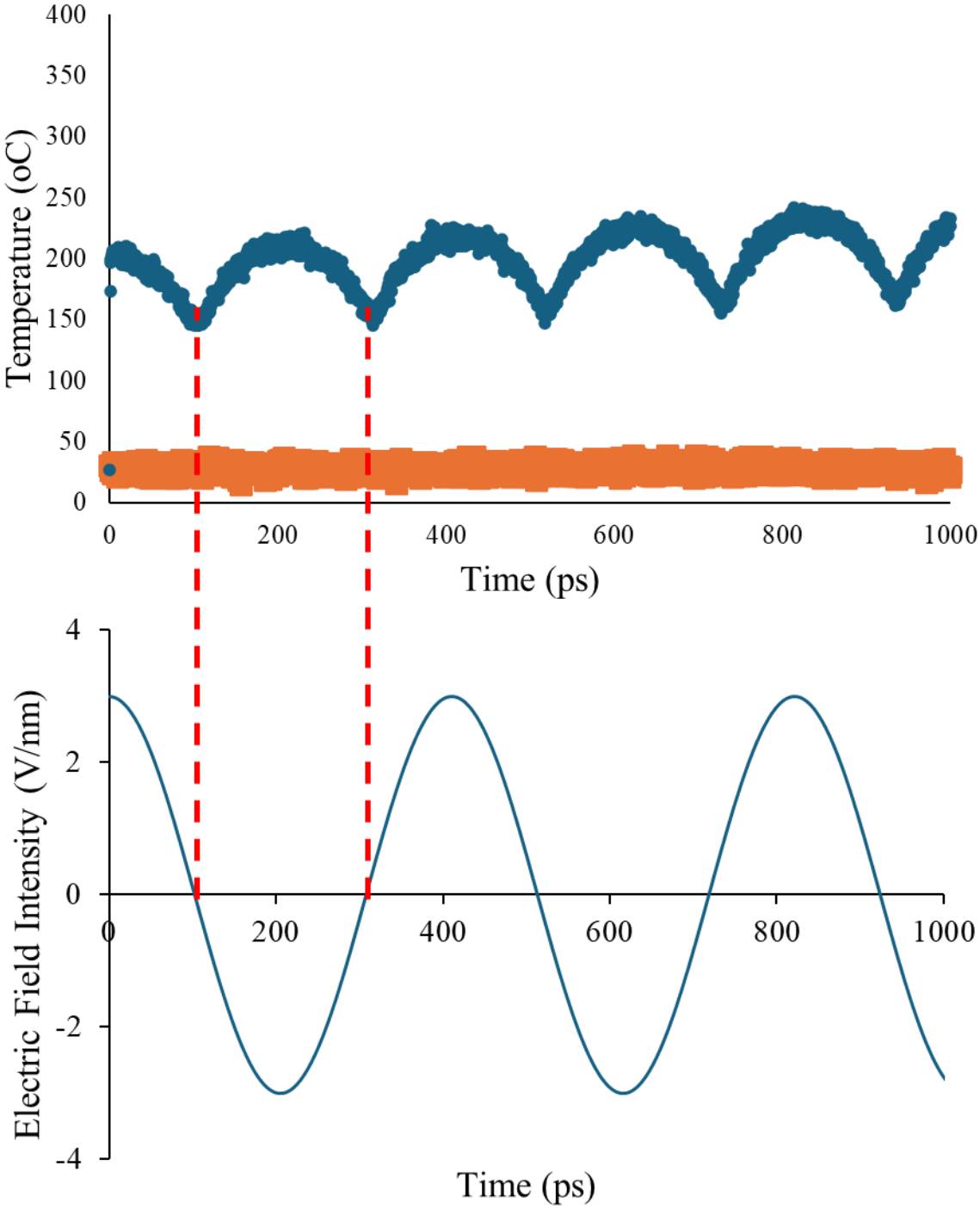

Figure 3-9 Temperature evolution for water (blue) and cyclohexane (orange) in respective monophasic system for 1 ns and the corresponding electric field wave at 2.45 GHz. Dashed red lines represent the same time for both graphs.

Since the oscillatory behaviour was observed for the water temperature evolution, the decrease in the temperature can be analyzed in relation to the change in volume under an

electric field of 2.45 GHz and 3.0 V/nm, as depicted in Figure 3-10. . For a system under constant pressure, the decrease in temperature after its fast initial increase, as observed also in Figure 3-9, is accompanied by an increase in volume at a constant potential energy. This is a somewhat interesting observation as the volume is expected to decrease with decreasing temperature at constant pressure. However, this system, is under an electric field. In Figure 3-10, it is also observed that the peak of the volume is directly aligned to the lowest point of the temperature for that oscillation period. The overall volume increases along with the temperature of the system.

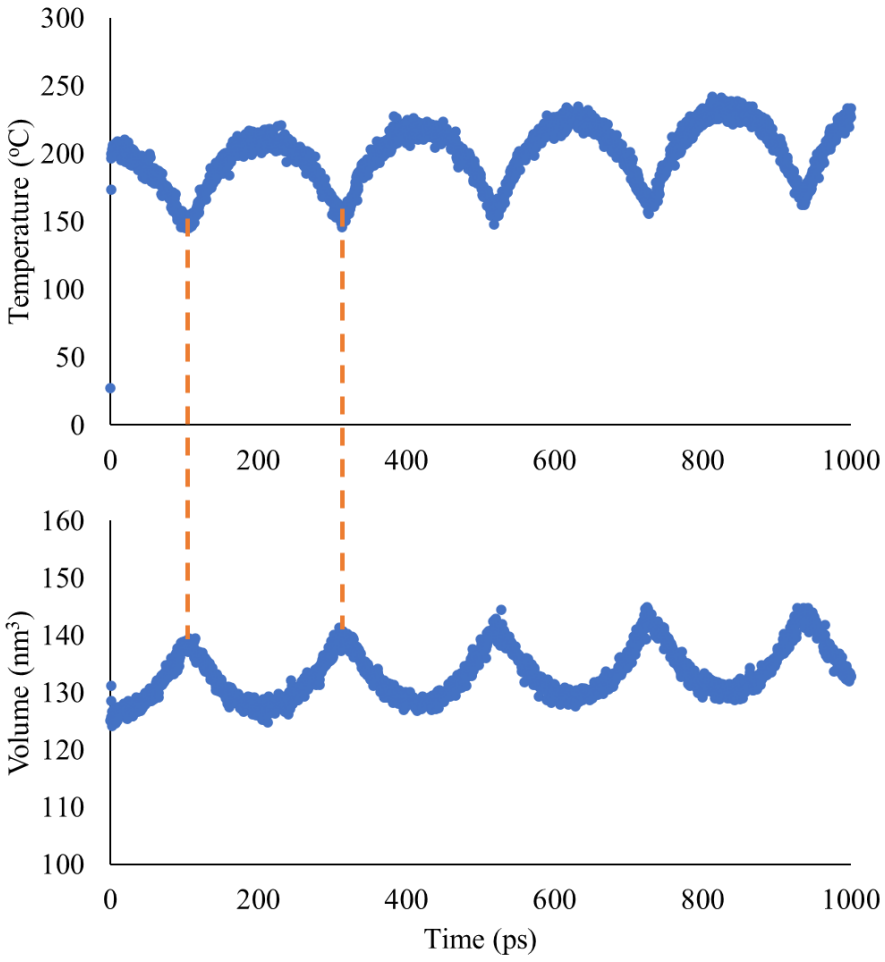

Figure 3-10 Temperature and volume evolutions for water in monophasic system for 1 ns subjected to an electric field of 3.0 V/nm and 2.45 GHz at a constant pressure of 1 bar. Dashed red lines represent the same time for both graphs.

The potential energy for the water system under the electric field of 2.45 GHz and 3.0 V/nm is presented in Figure 3-11. It shows that, for each period of the oscillation, the potential energy stays constant. The constant potential energy is aligned to the decrease in temperature found for each period and the increase in volume. After a period of electric field oscillation, the potential energy increases to a new plateau.

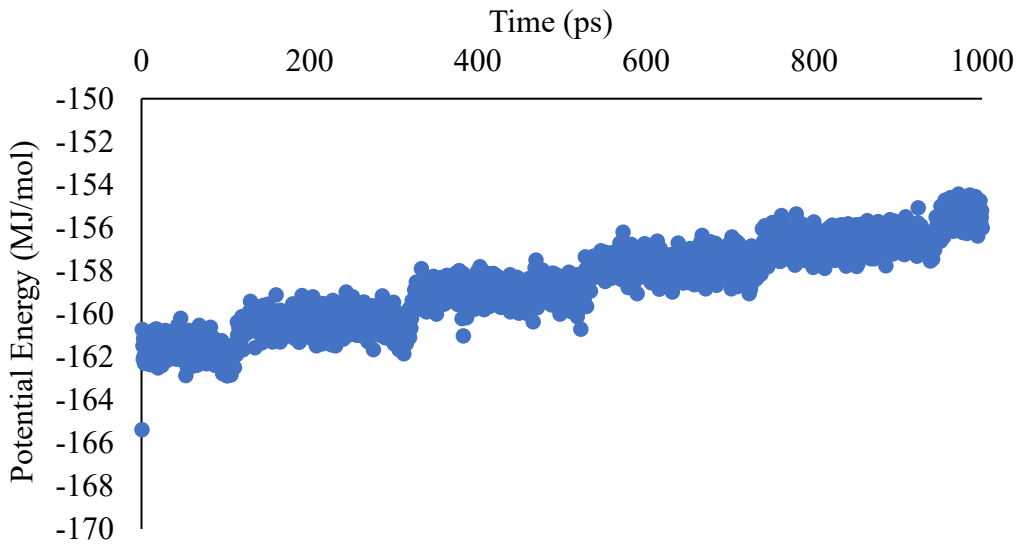

Figure 3-11 Potential energy evolution for water in monophasic system for 1 ns subjected to an electric field of 3.0 V/nm and 2.45 GHz at a constant pressure of 1 bar.

Although the potential energy remains constant for the period of time, the kinetic energy follows a similar behaviour to that of the temperature evolution, as shown in Figure 3-12. The kinetic energy and the temperature are expected to be aligned since both are variables calculated based on the particle velocities, as shown in Eq. 1-9.

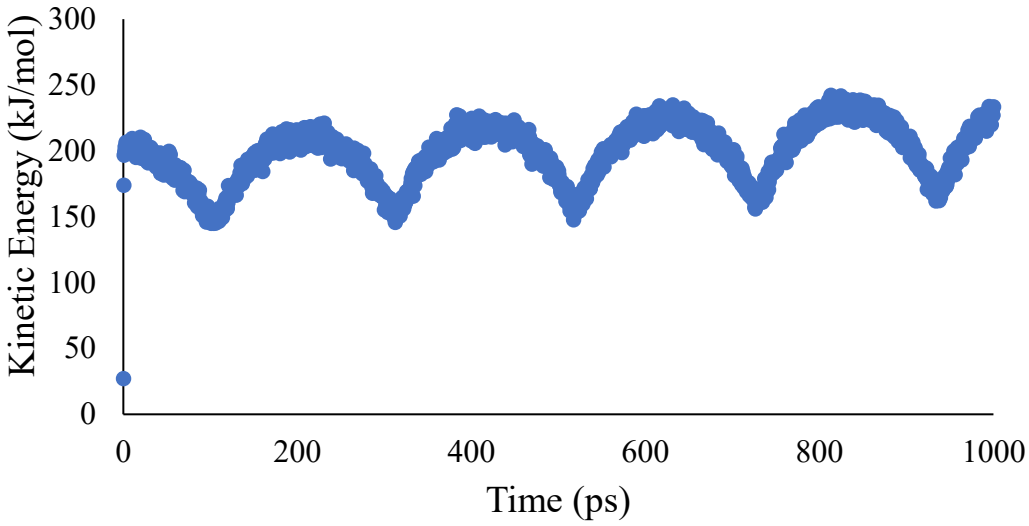

Figure 3-12 Kinetic energy evolution for water in monophasic system for 1 ns subjected to an electric field of 3.0 V/nm and 2.45 GHz at a constant pressure of 1 bar.

Simulations using 3.0 V/nm and 100 GHz were also carried out for water and cyclohexane, as shown in Figure 3-13. The temperature increase rate was much higher than those observed in Figure 3-6 and Figure 3-7, and the temperature of water increased to 1000ºC during of the initial 30 ps of the simulation. One distinct feature of the heating curve was its wave-like behaviour that can be related to the frequency used, similarly to the behaviour found in Figure 3-8 and Figure 3-9. For all frequencies studied, cyclohexane exhibited no temperature change (i.e., it was transparent to microwave radiation).

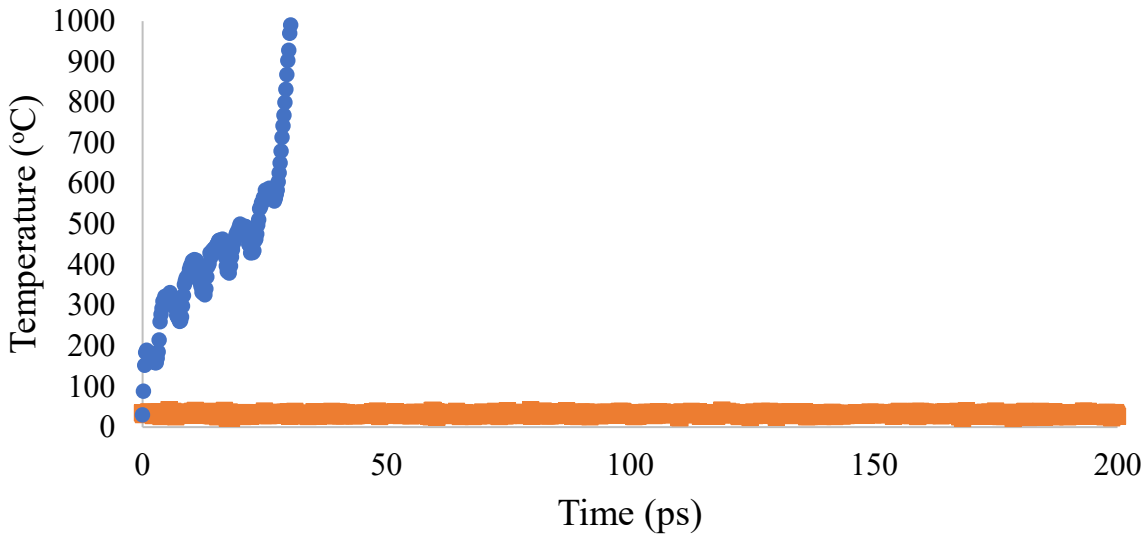

Figure 3-13 Comparison between the temperature evolutions of water (blue) and cyclohexane (orange) in respective monophasic systems subjected to an electric field of 3.0 V/nm and 100 GHz at a constant pressure of 1 bar.

When the electric field strength was high (i.e., 3.0 V/nm), water was heated up to 200°C in the first couple of picoseconds. In Figure 3-14, the temperature increase behaviours of water at three frequencies of 915 MHz, 2.45 GHz, and 100 GHz were compared.

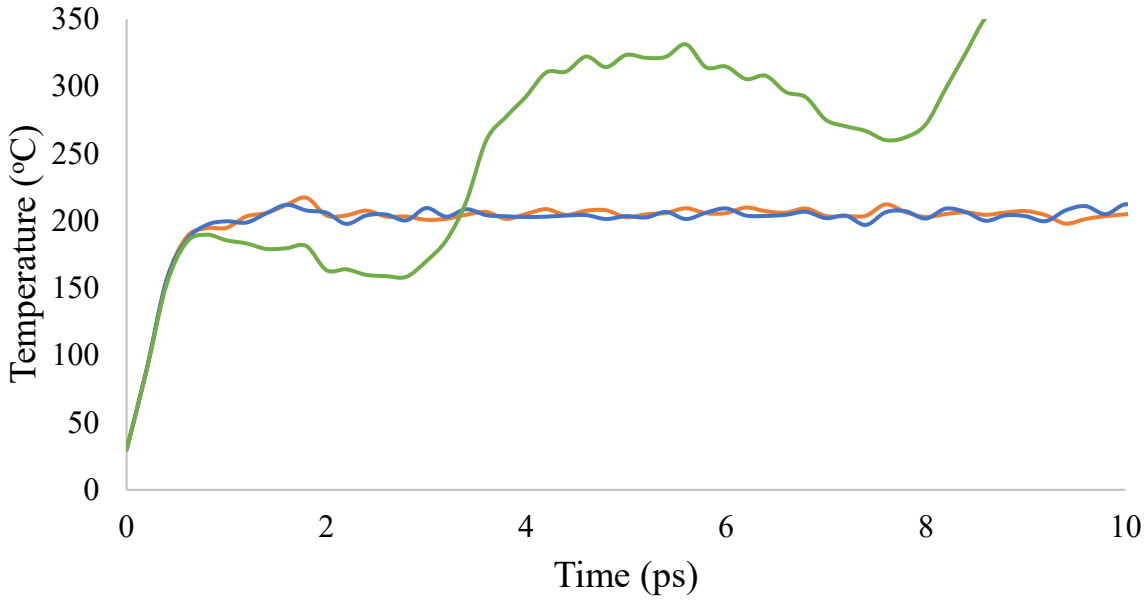

Figure 3-14 Comparison between the heating curves of pure water subjected to an electric field of 3.0 V/nm and 915 MHz (orange), 2.45 GHz (blue), and 100.0 GHz (green) at a constant pressure of 1 bar.

3.1.2 *Constant Volume Simulations*

Since Eq. 1-3 described a microwave heating process, in which the density of the substance was constant, and the above simulations were carried out under constant pressure, we also decided to carry out the MD simulations under constant volume conditions. The investigation of electric field heating under constant volume is often reported in literature (English, 2006; Shi et al., 2023). The results of the monophasic systems simulated under the constant volume condition show similar behaviour to those under the constant pressure condition, except the one using 100 GHz, as demonstrated in Figure 3-15, Figure 3-16, Figure 3-17.

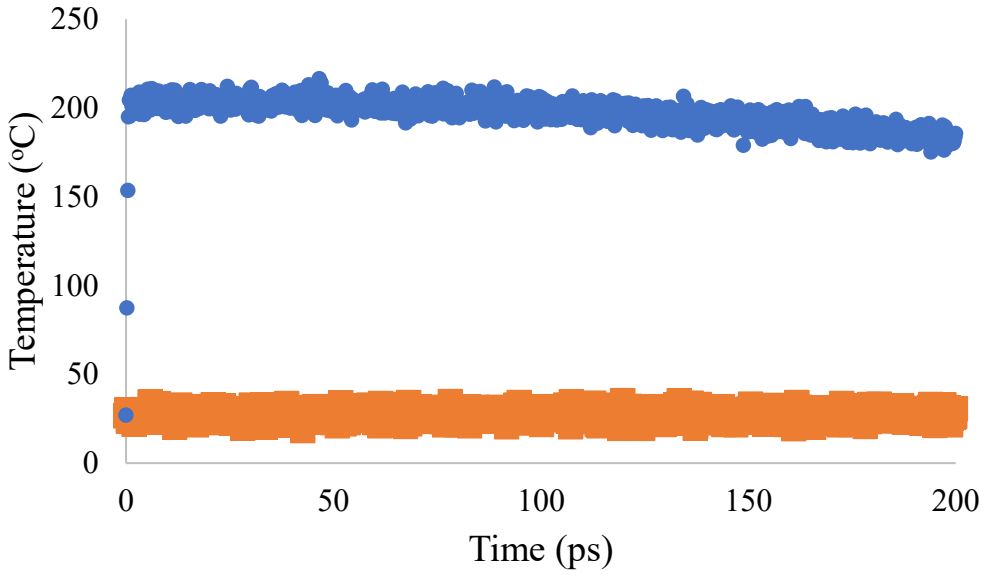

Figure 3-15 Temperature evolutions of water (blue) and cyclohexane (orange) in monophasic systems subjected to an electric field of 3.0 V/nm and 915 MHz, and a constant volume of 150 nm^3.

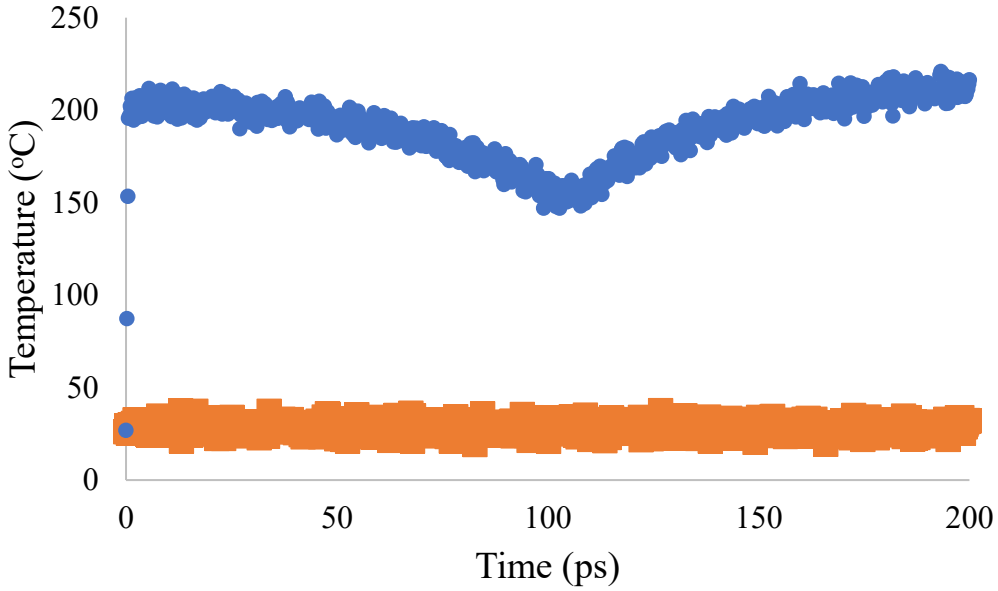

Figure 3-16 Temperature evolutions of water (blue) and cyclohexane (orange) in monophasic systems subjected to an electric field of 3.0 V/nm and 2.45 GHz, and a constant volume of 150 nm^3.

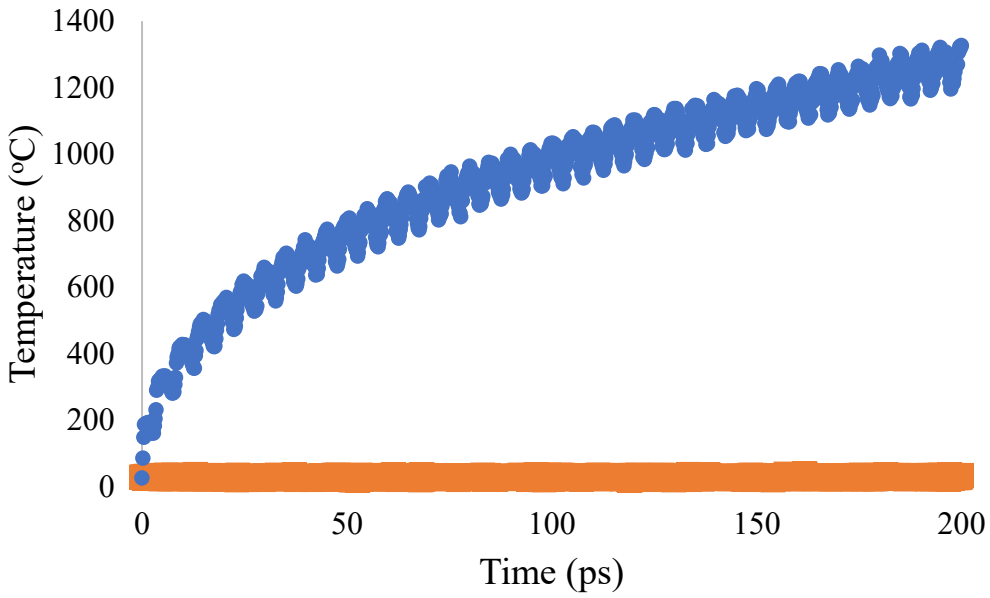

Figure 3-17 Temperature evolutions of water (blue) and cyclohexane (orange) in monophasic systems subjected to an electric field of 3.0 V/nm and 100 GHz, and a constant volume of 150 nm^3. The moving averages of the two systems are shown in lighter colors.

The difference between Figure 3-13 and Figure 3-17 can be attributed to the distinct constant pressure and constant volume conditions. This behaviour can be interpreted based on the change in the unit cell's volume, when a constant pressure is applied. The increase in volume allows molecules to have a higher velocity as the temperature increases. However, the constant volume simulation restricts the movement of water molecules, which impacts the velocities and, consequently, the temperature. Under constant volume conditions, the heating curve of water exhibits a regular temperature oscillation synchronized with the electric field frequency, as elaborated in Figure 3-8 and Figure 3-9, and the associated discussion in section 3.1.1.

3.1.3 Rotational Autocorrelation Function

The observed temperature change of the monophasic water and cyclohexane systems show the interaction between the dipole behaviour of water molecules and the imposed electric

field. The molecular rotational motion can be characterized by the RAF, as previously mentioned in Eq. 1-43, which represents the difference in rotation of the molecular axis between the unit cell structure at time t_0 (initial structure) and time t (current structure). The time evolution of RAF can be interpreted as the rate at which the system changes from its initial state, and denotes the effect of the imposed electric field on the rotation of molecules. In the figures that illustrate the RAF analysis, the faster decrease in RAF (C_R^2) indicates a faster rotational motion, which in the presence of electric field is attributable to faster heating, since the temperature is related to the particles' momenta by Eq. 1-7.

For the monophasic system of water under constant pressure, the RAF analysis performed in electric field with a strength of 3 V/nm shows a behaviour similar to the temperature evolution results. Figure 3-18 shows that the RAF decreases faster as electric field is applied and its frequency is increased.

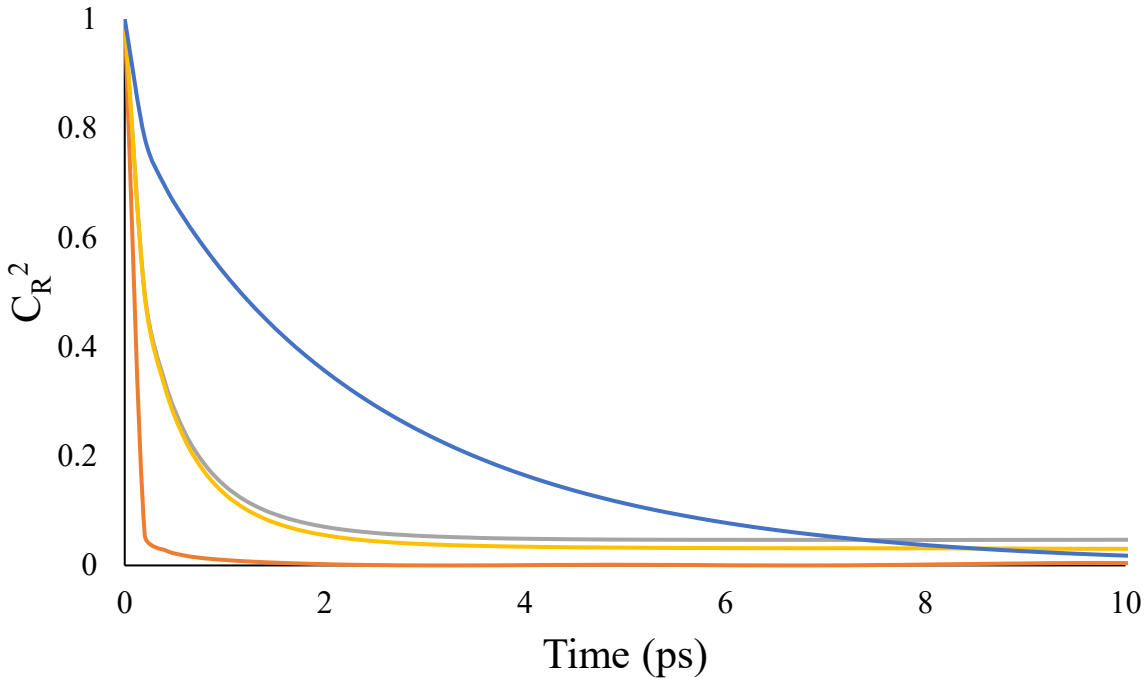

Figure 3-18 Evolution of the RAF of molecules in a monophasic water system that are under no electric field (blue) and with electric field strength of 3 V/nm at frequencies of 915 MHz (grey), 2.45 GHz (yellow), and 100 GHz (orange) at constant pressure of 1 bar.

The RAF results clearly show the effect of the electric field on the rotational motion of water molecules, associating its impact on molecules with a strong dipole moment. The application of 2.45 GHz and 915 MHz causes comparable effect, with both exhibiting a faster drift compared to the simulation without any external field applied. Simulation with 100 GHz leads to a fast decorrelation in the rotational motion of the water molecules, which is in agreement with the temperature evolution in Figure 3-13. The overall RAF behaviour trends strongly agree with the temperature evolution of water, shown in Figure 3-14.

The RAF analysis performed for the constant pressure condition on a cyclohexane monophasic unit cell exhibits essentially no difference in the rotation decorrelations, when the simulations with and without an electric field are compared. The results shown in Figure 3-19 show an overlap of the simulations with all 3 frequencies applied in this study and the

simulation without any external field. The RAF analysis of cyclohexane highlights its transparency to the electric field and shows that this molecule is not affected by the electric field strength and frequency.

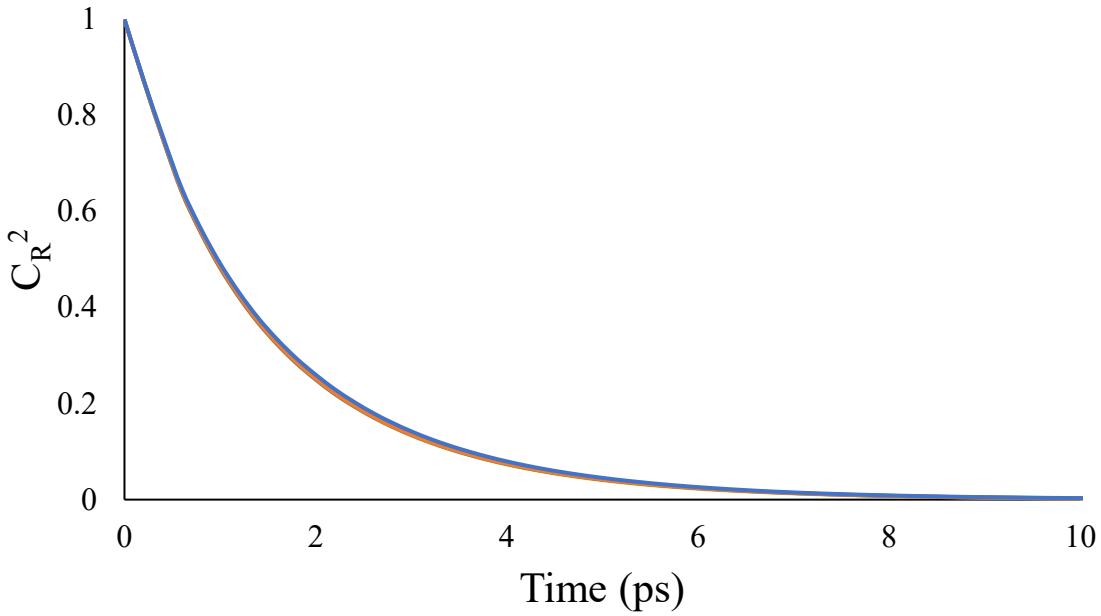

Figure 3-19 Evolution of the RAF of monophasic cyclohexane system that are under no electric field (blue) and with electric fields strength of 3 V/nm at frequencies of 915 MHz (orange), 2.45 GHz (green) and 100 GHz (grey) at constant pressure of 1 bar. All curves overlap.

The distinct behaviors of the RAF of water and cyclohexane can be seen in Figure 3-20, where the water molecules change from their initial state rapidly upon the application of electric field with increasing strength. The results also highlight that water generally undergoes slower rotational motion than cyclohexane in the absence of electric field, likely due to water's inherent hydrogen bonding.

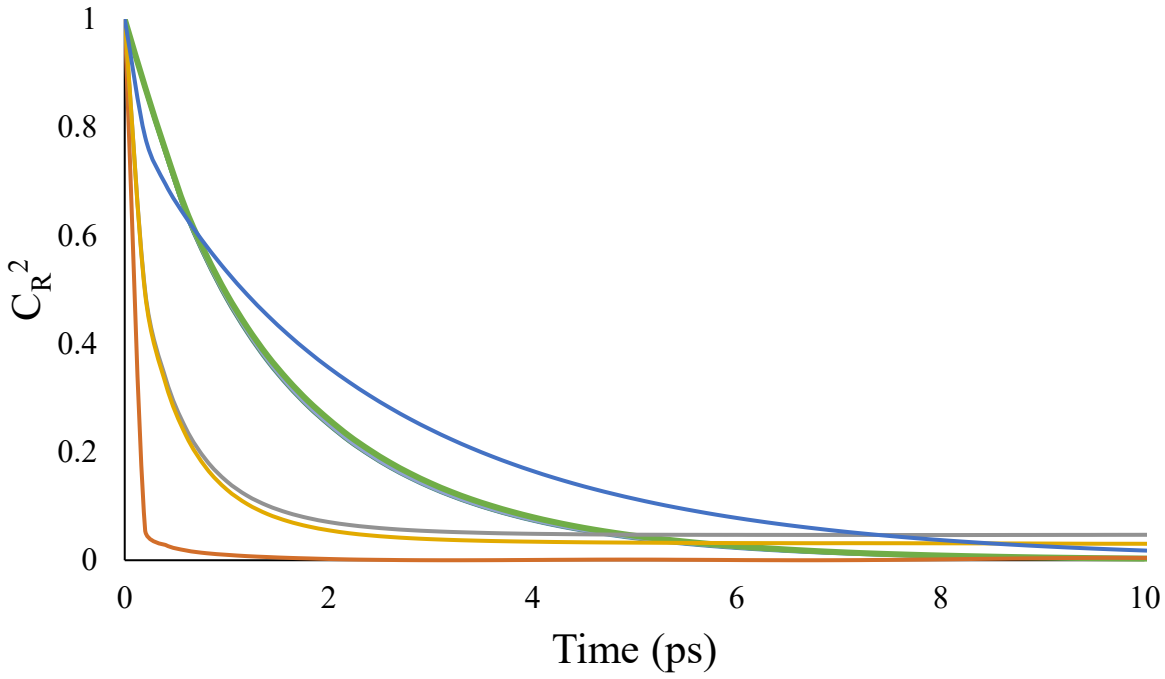

Figure 3-20 Evolution of the RAF of monophasic water and cyclohexane systems that are under no electric field (blue for water) and with electric field strength of 3 V/nm and at frequencies of 915 MHz (grey), 2.45 GHz (yellow) and 100 GHz (orange) for the water system at constant pressure of 1bar. The green curve denotes the results of cyclohexane without and with imposed electric fields.

3.2 Biphasic Systems Containing Water and Cyclohexane

The biphasic systems were simulated following the structure in Figure 2-2 using ~50 nm^3 of water and ~100 nm^3 of cyclohexane assembled right next to each other, as exemplified in Figure 2-2. For these simulations, the thickness of the water layer was 2.5 nm, while the thickness of the cyclohexane layer was 4.5 nm.

3.2.1 *Constant Pressure Simulations*

The electric field used had a strength of 0.01 V/nm and a frequency of 2.45 GHz. Figure 3-21 shows that water (blue) and cyclohexane (orange) do not exhibit notable temperature increase despite small temperature fluctuations for both liquids. It is interesting to note that the

temperature fluctuations of water and cyclohexane occur in opposite directions, suggesting that the energy absorbed by the water molecules from the microwave is transferred to the cyclohexane molecules through their molecular motion. The energy transfer process leads to the two liquids' temperature changes being anticorrelated.

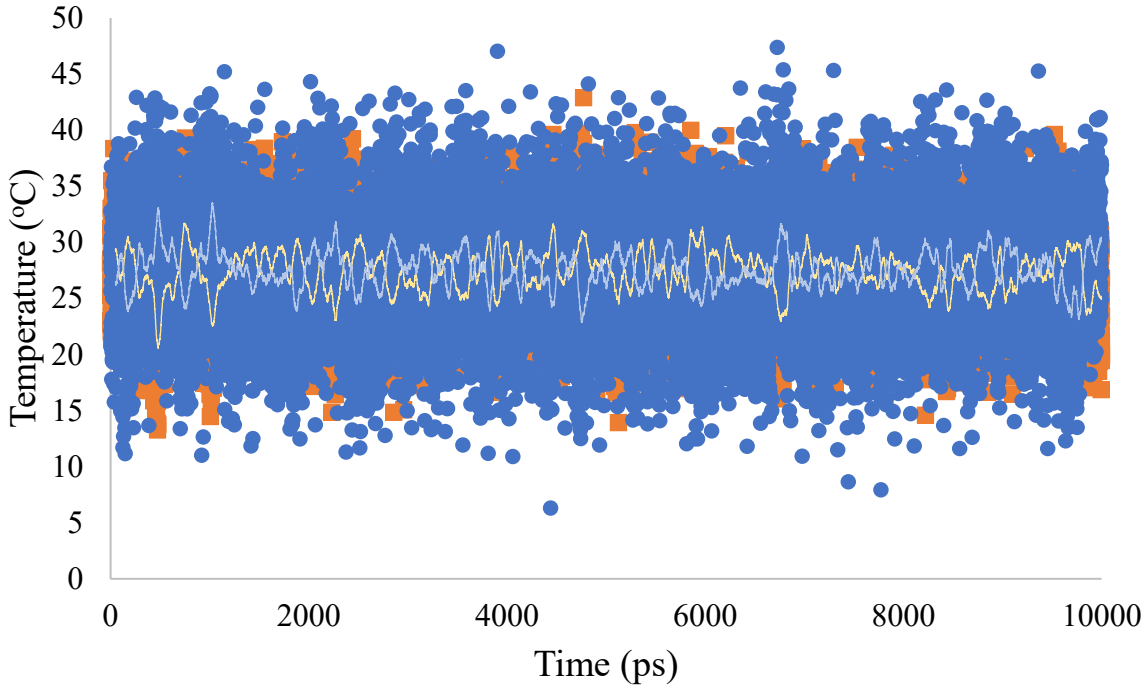

Figure 3-21 Temperature evolutions of water (blue) and cyclohexane (orange) in a biphasic system subjected to an electric field of 0.01 V/nm and 2.45 GHz at a constant pressure of 1 bar. The moving averages of the two systems are shown in lighter colors.

Figure 3-22 shows the time evolutions of the temperatures of water and cyclohexane throughout 10 ns in the biphasic system subjected to an electric field of 0.01 V/nm and 100 GHz. Both liquids exhibit temperature increase. The temperature increase for water is moderate compared to the water monophasic system shown in Figure 3-5. The temperature of cyclohexane increases because of the energy transfer from water to cyclohexane. Once again, the fluctuations of water and cyclohexane occur in the opposite directions.

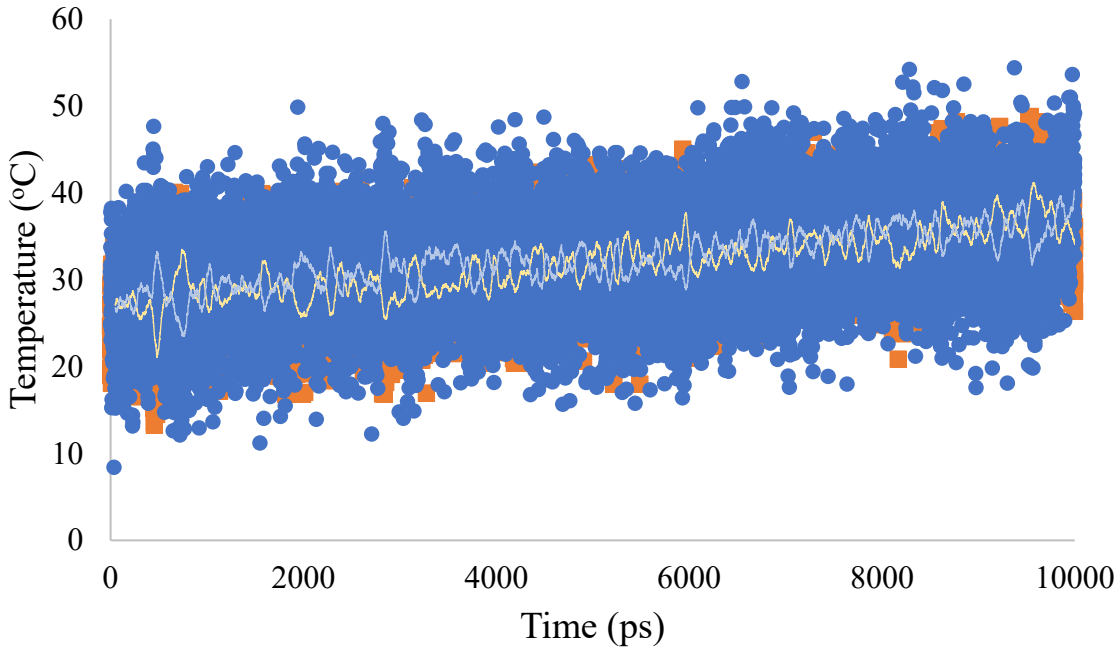

Figure 3-22 Temperature evolutions of water (blue) and cyclohexane (orange) in a biphasic system subjected to an electric field of 0.01 V/nm and 100 GHz at a constant pressure of 1 bar. The moving averages of the two systems are shown in lighter colors.

The biphasic system simulation was also performed using a higher electric field strength of 3.0 V/nm at the three frequencies of 915 MHz, 2.45 GHz and 100 GHz, as done for the monophasic system. Figure 3-23 shows the time evolutions of the temperatures of water (blue), cyclohexane (orange), and the entire biphasic system (grey) upon the application of an electric field with a strength of 3.0 V/nm and frequency of 915 MHz. Clearly, the temperature increase of water and cyclohexane using an electric field strength of 3.0 V/nm are higher than those in the simulation using an electric field strength of 0.01 V/nm. From 5 to 50 ns, there is a gap between the water and cyclohexane temperature curves (see Figure 3-23, inset), indicating that water is warmer than cyclohexane as a result of its faster heating due to microwave adsorption. The increase of the temperature of cyclohexane, which is distinct from the behavior of the monophasic cyclohexane system (see in Figure 3-6) suggests that there is heat transfer from water to cyclohexane. Water and cyclohexane reach peak temperatures of 120°C and 80°C,

respectively, at around 15 ps. It should be noted that given the setup of the simulation unit cell, no phase transition (evaporation) takes place even though water and cyclohexane reach their experimental boiling points (100ºC and 80ºC) under pressure used (1 atm). After reaching their peak temperatures, both liquids approach the same plateau temperature of 110ºC at about 50 ps. This thermal equilibration process demonstrates that energy is transferred from water to cyclohexane, as cyclohexane is microwave-transparent. The temperature plateau is reached after a decrease in temperature from the water system and an increase in temperature from the cyclohexane. The increase in the overall temperature is observed, as mentioned in Figure 3-8 and Figure 3-9, following the same electric field peaks. The peaks found for the cyclohexane molecules are associated with the thermal equilibrium.

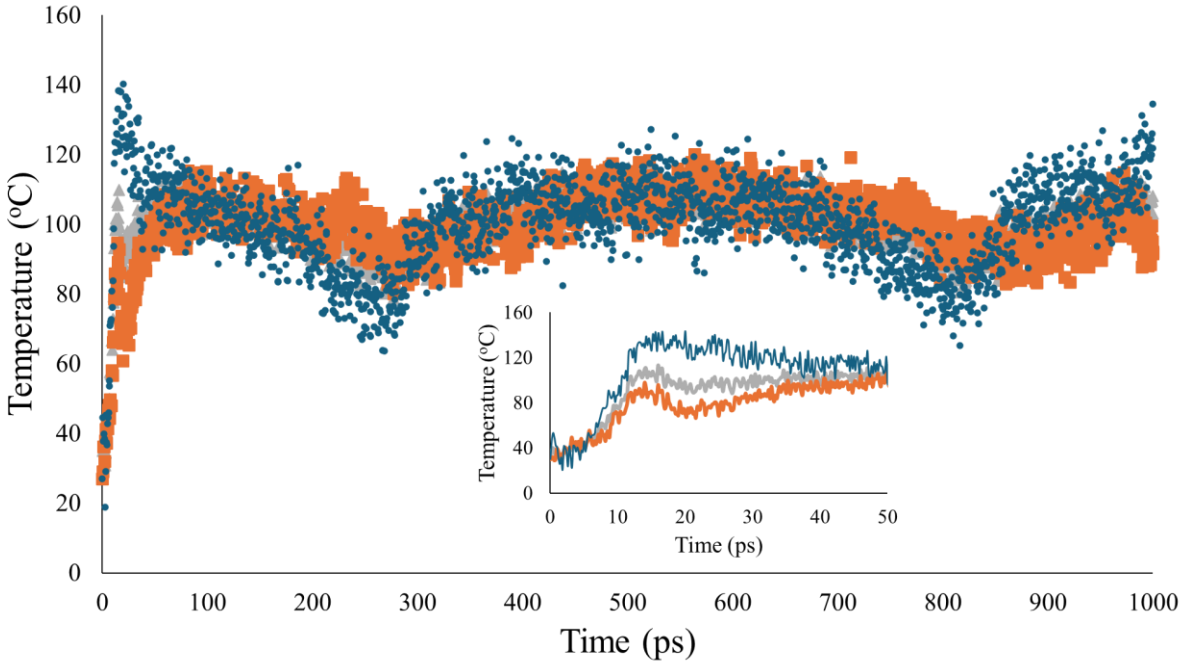

Figure 3-23 Temperature evolutions of water (blue), cyclohexane (orange) and entire system (grey) in a biphasic system subjected to an electric field of 3.0 V/nm and 915 MHz at a constant pressure of 1 bar.

Figure 3-24 shows the results using microwave with a frequency of 2.45 GHz. Once the temperatures of water and cyclohexane have reached their peaks, observed in the inset of Figure

3-24 they start to decrease followed by temperature increase as observed in the water monophasic system (see Figure 3-7). and Figure 3-25, as the higher water temperature can be seen to start around 8 to 12 ps. The biphasic system presents the temperature increase of cyclohexane unlike the behaviour found on the monophasic analysis shown in Figure 3-7 and its occurrence following the same heating behaviour of the water molecules.

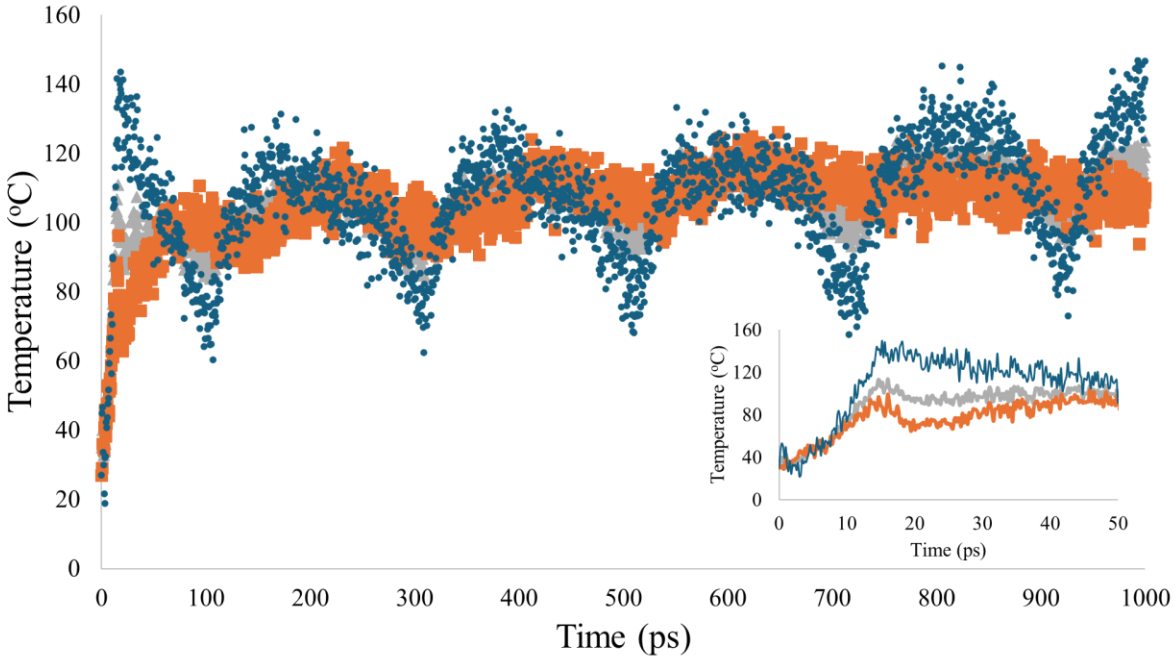

Figure 3-24 Temperature evolutions of water (blue), cyclohexane (orange) and entire system (grey) in a biphasic system subjected to an electric field of 3.0 V/nm and 2.45 GHz at a constant pressure of 1 bar.

The MD simulation results for the biphasic system using 3.0 V/nm and 100 GHz are shown in Figure 3-25. Given the rapid heating due to the high frequency, results only up to 40 ps are shown. Water in this biphasic system shows similar behaviour to that depicted in Figure 3-13, but the temperature increase rate is lower as some energy is transferred to cyclohexane. However, the higher frequency increases the water temperature faster than the energy transfer to the cyclohexane, leading to a more significant gap between the temperature curves of the

two liquids. The temperature of the cyclohexane slowly increases towards the temperature of the water.

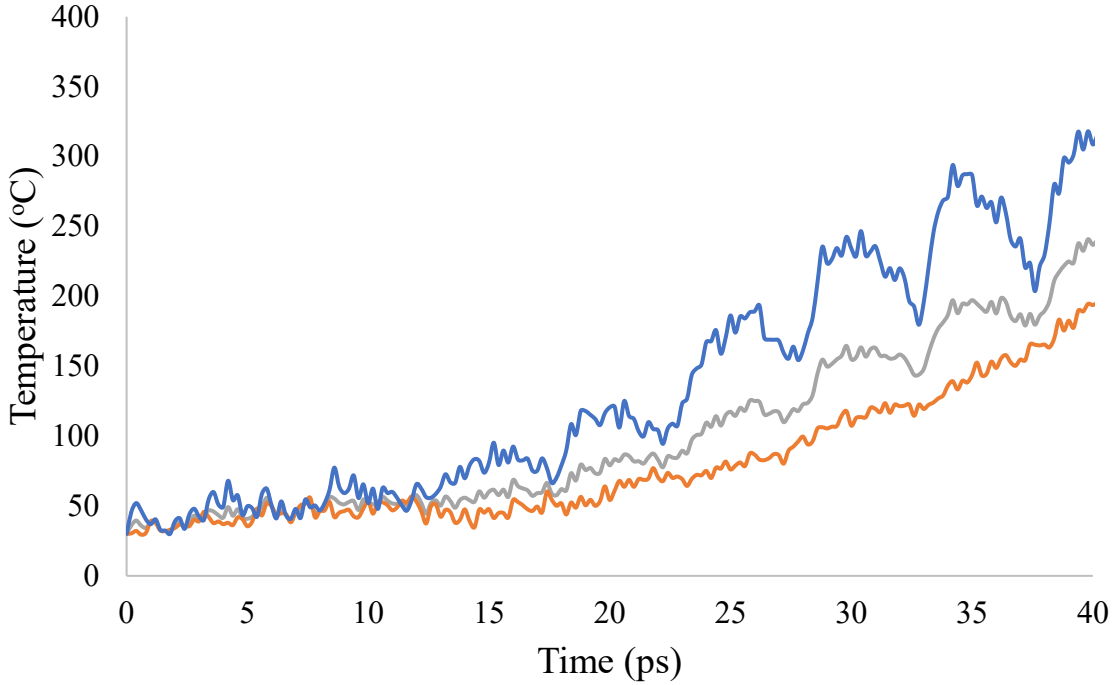

Figure 3-25 The temperature evolutions of water (blue), cyclohexane (orange) and entire system (grey) in a biphasic system subjected to an electric field of 3.0 V/nm and 100 GHz at a constant pressure of 1 bar.

3.2.2 *Constant Volume Simulations*

In the case of the biphasic system under the constant volume condition, the results (Figure 3-26 and Figure 3-27) differ from those under constant pressure, as shown in Figure 3-23 and Figure 3-24. In particular, cyclohexane does not show any temperature decrease over the course of the simulations. The difference between the temperature for the water system compared to the cyclohexane has increased when using a lower frequency, 915 MHz, which can result from a more extended period on the peak intensity of the electric field.

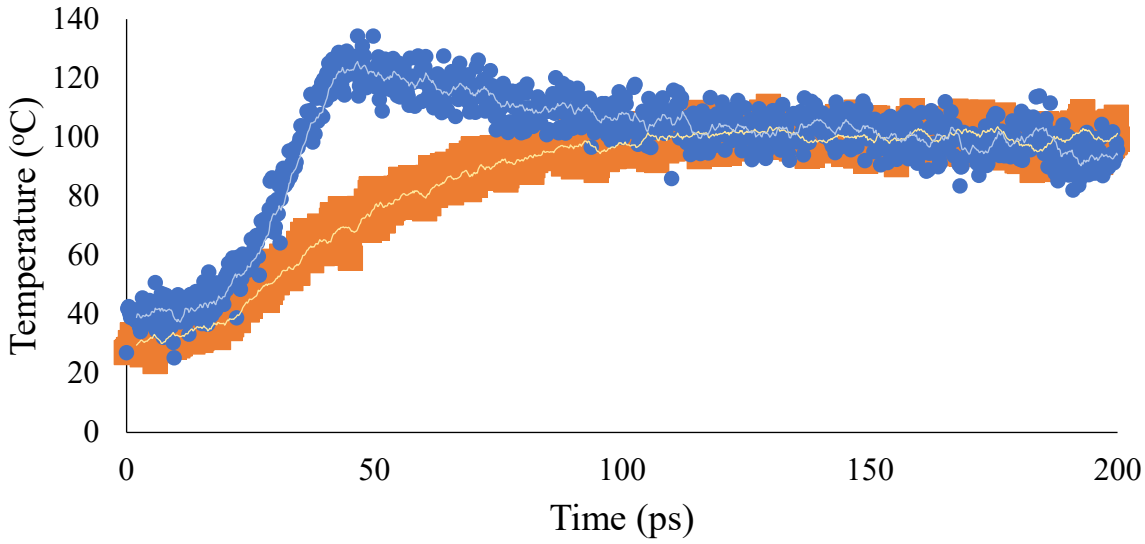

Figure 3-26 The temperature evolutions of water (blue) and cyclohexane (orange) in a biphasic system subjected to an electric field of 3.0 V/nm and 915 MHz, and a constant volume of 150 nm^3.

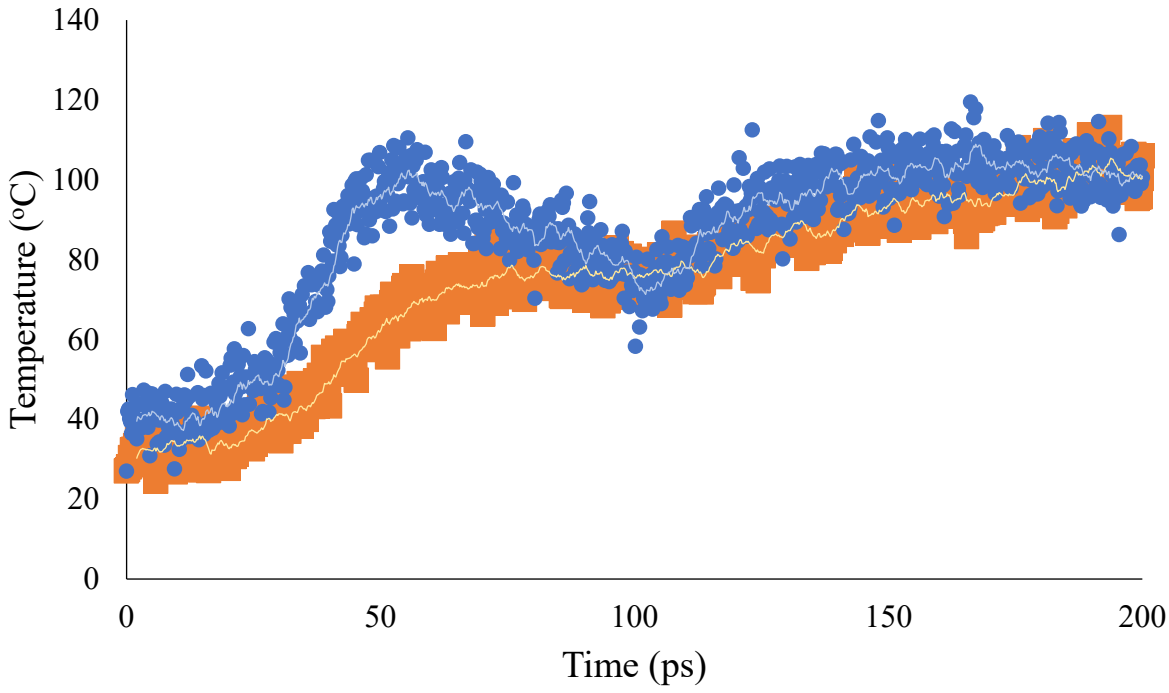

Figure 3-27 The temperature evolutions of water (blue) and cyclohexane (orange) in a biphasic system subjected to an electric field of 3.0 V/nm and 2.45 GHz, at a constant volume of 150 nm^3.

For the simulation using 100 GHz frequency, throughout the simulation (200 ps), the water temperature reaches a lower value than that under constant pressure conditions. Figure 3-28 shows that oscillation exists in water temperature, but this is not the case for cyclohexane. The oscillation exhibited by the water temperature profile is due to the high frequency, which allows the water molecules to increase the temperature faster than the energy transfer to the cyclohexane that steadily increases towards the water temperature. The cyclohexane reaches the equilibrium temperature of 915 MHz and 2.45 GHz.

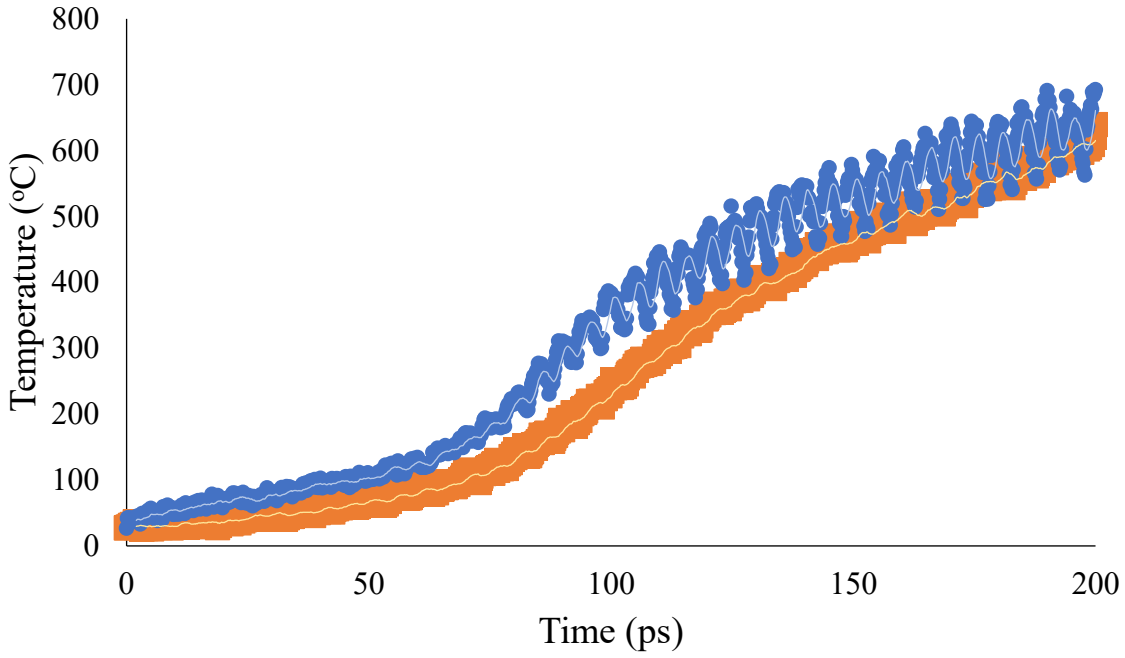

Figure 3-28 The temperature evolutions of water (blue) and cyclohexane (orange) in a biphasic system subjected to an electric field of 3.0 V/nm and 100 GHz and a constant volume of 150 nm^3.

3.2.3 Rotation Autocorrelation Function and Mean Square Displacement

For the biphasic systems under constant pressure, the RAF results show that the rotational decorrelation times of water and cyclohexane are about the same (~2 ps). Indeed, the decorrelation time of cyclohexane is significantly decreased, indicating that there is a

significant increase in it rotational motion (see Figure 3-29). However, the rotational decorrelation of water molecules is similar to that of them in monophasic systems.

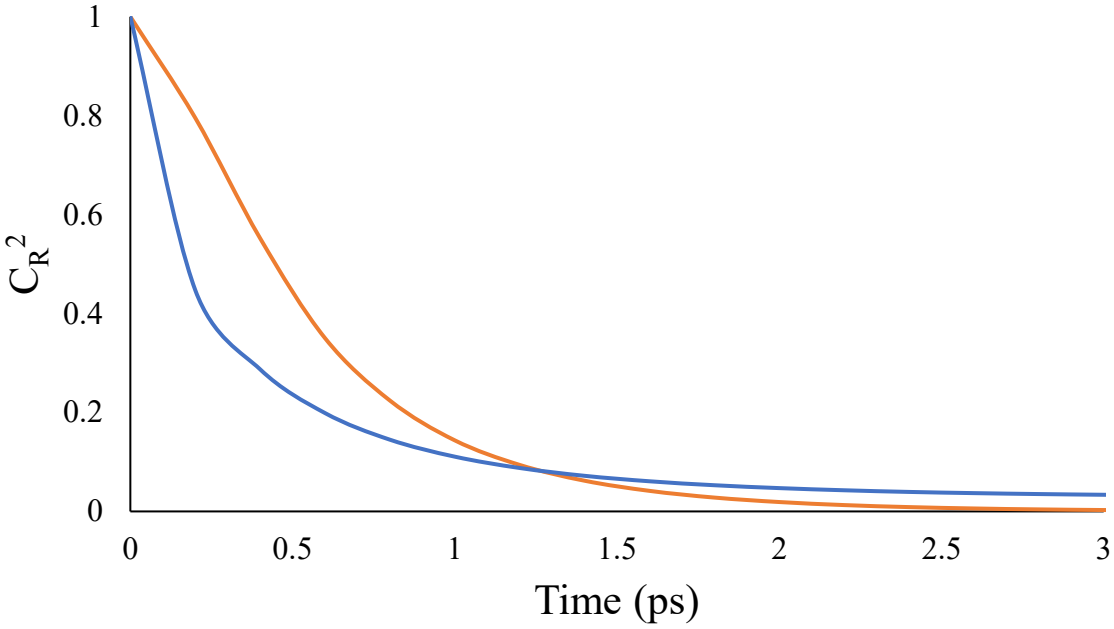

Figure 3-29 Evolution of the RAF of water (blue) and cyclohexane (orange) in biphasic system that is under an electric field at a frequency of 2.45 GHz and electric field strength of 3 V/nm at a constant pressure of 1 bar.

The RAF data elucidates the mechanism of energy transfer between water and cyclohexane. After absorbing energy from the electric field, water molecules increase their rotational motion, shortening their rotational decorrelation time. As a result, this energy is transferred to cyclohexane molecules, thereby shortening their rotational decorrelation time. The combination of the observed rotational and the translational motions of cyclohexane promotes the temperature change seen in the temperature evolution analysis previously discussed.

To compare the energy transfer mechanism, Figure 3-30 shows the rotation for the monophasic systems of water and cyclohexane and its behaviours for the biphasic analysis, with a clear distinction between the monophasic and biphasic cyclohexane RAF.

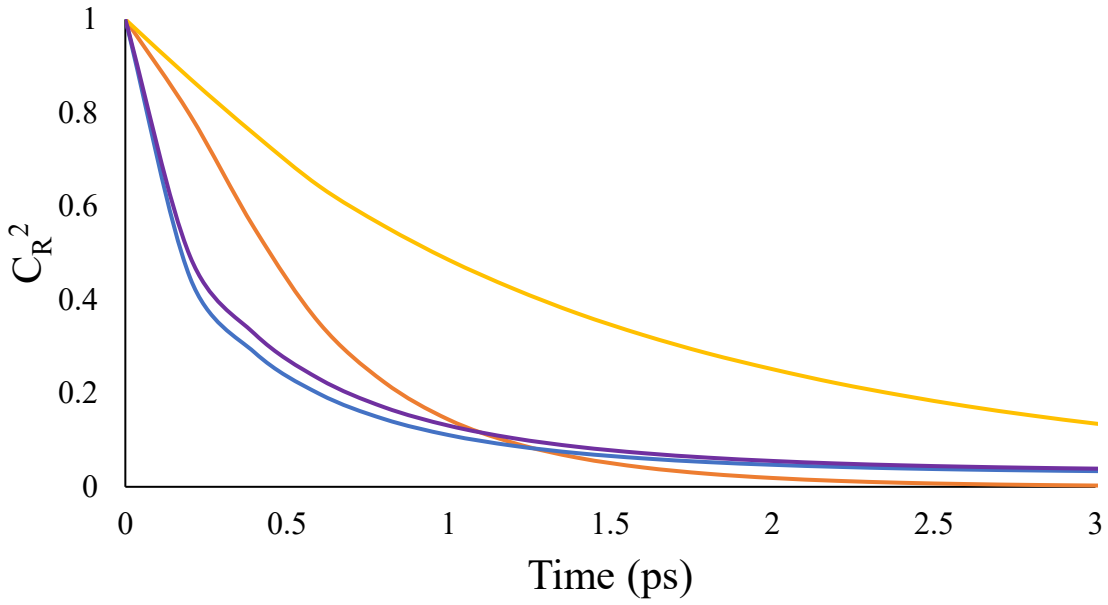

Figure 3-30 Evolution of the RAF of water (blue) and cyclohexane (yellow) in monophasic system considering the simulation with electric field strength of 3.0 V/nm and frequency of 2.45 GHz at a constant pressure of 1 bar. The biphasic system water is represented in purple and the cyclohexane in orange to represent the energy transfer effect.

The correlation between the evolution of the RAF and the translational motion of water and cyclohexane is observed by the MSD analysis and the diffusion coefficient D found for monophasic and biphasic systems. As the diffusion is related to the velocities as mentioned in Eq. 1-44, the Figure 3-31 shows the coefficients *D* for mono- and biphasic water and cyclohexane with and without electric field, indicating an increase in the diffusion of cyclohexane in the biphasic system in comparison to the monophasic system after imposing an electric field. This behaviour is related to the heating mechanism from water to the cyclohexane. It is also observed that the water diffusion decreases when comparing the biphasic

to the monophasic water system. This decrease has the same relation as the RAF for the water molecules, observed in Figure 3-30.

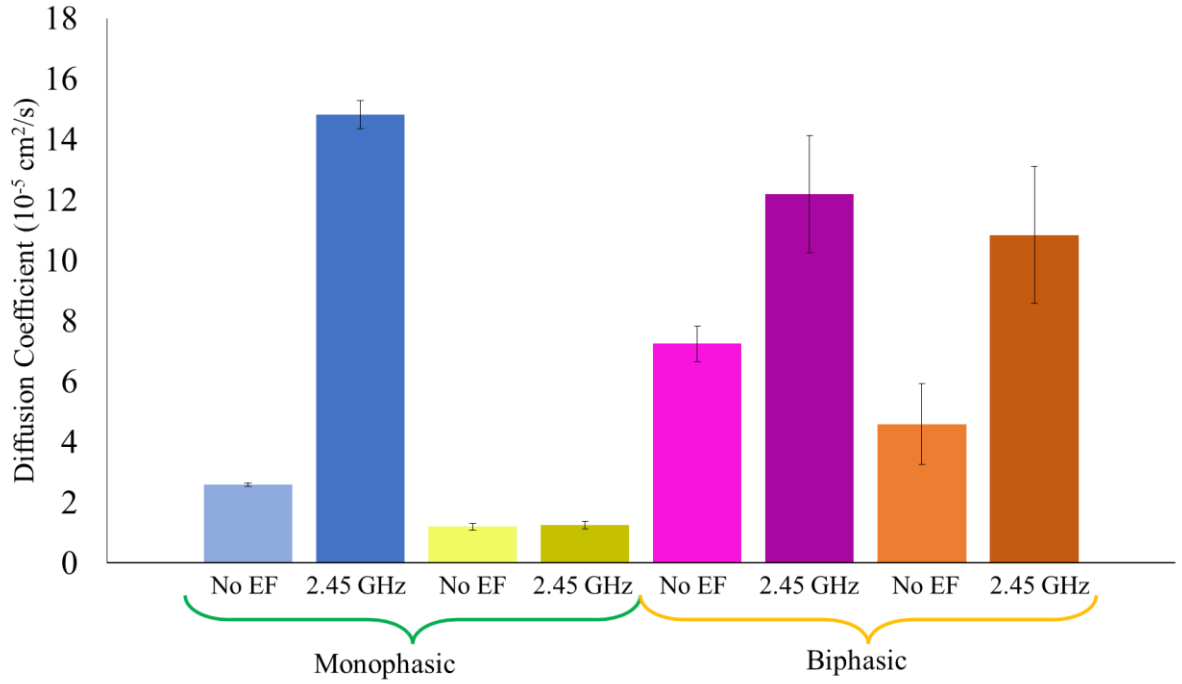

Figure 3-31 Diffusion coefficients of water in monophasic (blue) and biphasic systems (purple), and cyclohexane in monophasic (yellow) and biphasic (orange) systems, simulated with no electric field (light colours) and, in dark colours, simulation with electric field strength of 3.0 V/nm and frequency 2.45 GHz at a constant pressure of 1 bar. The respective errors provided by the linear fit performed by the software are included in the graph.

4 Conclusion

Owing to the negative environmental impact of the current water-based oil sands extraction process, a NAE process has been developed. In comparison to the mining and SAGD extraction, the NAE is defined by the use of organic solvent for the bitumen extraction. The use of an organic solvent, such as the cyclohexane, creates a new challenge as the resulting gangue contains residue solvent that need to be removed. Conventional heating is not energy efficient as it is not targeted. Microwave heating overcomes this drawback as it can be targeted.

In the microwave heating of gangue generated from the NAE, cyclohexane, the extraction solvent, is vaporized even though it is microwave transparent. It is believed that the connate water presented in the oil sands functions as a heating agent. However, it is difficult to study such a heat transfer process experimentally. Therefore, in this work, a commonly used molecular simulation technique, namely MD simulation, was used to study how cyclohexane is heated in the presence of water.

The work involved investigating how external electric fields with frequencies in the range of microwave heat water and cyclohexane in monophasic and biphasic systems. This study was performed using nanoscale models along with electric fields of various strengths to demonstrate heating at observable and applicable rates. The electric field was applied with frequencies of 915 MHz, 2.45 GHz, and 100 GHz, and electric field strengths of 0.01 and 3 V/nm. Since the length and time scales of the models differ from the macroscopic systems, primarily qualitative agreement was sought.

Simulations performed for the monophasic systems of water and cyclohexane under an electric field showed that water was heated up by the electric field, while cyclohexane was not. This was because water had a high dipole moment, whereas cyclohexane did not have a permanent dipole moment. The use of electric field with a strength of 0.01 V/nm demonstrated low heating for the water system; however, the application of a higher electric field strength (3 V/nm) for all frequencies yielded higher rates of temperature increase for water. Interestingly, the use of a very high frequency (100 GHz), higher than those used experimentally, yielded an increasing oscillatory temperature profile for water. The oscillatory temperature increase behaviour was also observed for 915 MHz and 2.45 GHz frequencies applied. The oscillations were attributed to the frequency of the electric field.

As mentioned, biphasic systems containing water and cyclohexane were used to simulate the coexistence situation in gangue. Here, owing to the immiscibility of the two liquids, the two different layers with one containing water (bottom of the unit cell) and the other layer cyclohexane (top of the unit cell), obeying their natural density values, were studied. Similar to the monophasic systems, the biphasic simulations were subjected to electric fields and the temperatures of the two liquids were monitored. Interestingly, even though cyclohexane was microwave transparent, it was also heated up in the biphasic systems, indicating the occurrence of energy transfer from water to cyclohexane. Although there was a lag in the cyclohexane temperature, both water and cyclohexane reached the same steady state temperature. The temperature difference between water and cyclohexane was observed after the use of high electric field strength of 3 V/nm, since the simulations with 0.01 V/nm did not present such behaviour.

The non-equilibrium MD simulations under constant pressure or constant volume condition showed that water absorbed energy from the imposed electric field and transferred some of it to cyclohexane. As a result, cyclohexane was also heated up. It was likely that the collision between the water and cyclohexane molecules at the interface led to the energy transfer. Nonetheless, the temperature of water in the biphasic systems was higher than that of cyclohexane, which was observed experimentally in microwave heating experiments.

The rotation autocorrelation function confirmed the energy transfer from the electric field to water molecules that exhibit a strong dipole moment. The monophasic and biphasic systems of water have shown increase on the rotation of molecules after the external field. The external field applied to cyclohexane has exerted no effect on the rotation autocorrelation function in the cyclohexane monophasic phase. The biphasic system exhibited alteration of the cyclohexane's rotational motion, which was caused from the water motion influenced by the

electric field, suggesting that there was energy transfer between water and cyclohexane molecules.

The change in the rotational to translational motion was then described by the MSD results and the diffusion coefficient calculated for water and cyclohexane mono- and biphasic systems. The diffusion expressed an increase in the cyclohexane translational motion and a decrease in that of water, which related to the behaviour found based on the RAF analysis. These molecular motion results were interpreted as being caused by the energy transfer from the promoted rotational motion of water molecules, due to the electric field, to the cyclohexane that was not affected by the imposed electric field.

The solvent recovery from gangue, an important step of the NAE, can be improved and optimized based the heating mechanism and temperature profile findings for the biphasic system in different simulation conditions. The overall temperature of the sample can be characterized by the rotational and translational motion of water and cyclohexane aligned with the temperature lag during the biphasic system heating. The heating mechanism determined in the study can be used to optimize the microwave heating for a gradual increase in the temperature of water and, consequently, an increase of the temperature of cyclohexane until it reaches its boiling point.

Bibliography References

Allen, M.P., Tildesley, D.J., 2017. Computer Simulation of Liquids. Oxford University Press. https://doi.org/10.1093/oso/9780198803195.001.0001

Ayappa, K.G., Davis, H.T., Davis, E.A., Gordon, J., 1992. Two-dimensional finite element analysis of microwave heating. AIChE J. 38, 1577–1592. https://doi.org/10.1002/aic.690381009

Barringer, S.A., Davis, E.A., Gordon, J., Ayappa, K.G., Davis, H.T., 1994. Effect of sample size on the microwave heating rate: Oil vs. water. AIChE J. 40, 1433–1439. https://doi.org/10.1002/aic.690400902

Bhatt, S.C., Ghetiya, N.D., 2022. Review on effect of tooling parameters on microwave processing of metallic materials with special emphasis on melting/casting application. Inter Metalcast 16, 2097–2127. https://doi.org/10.1007/s40962-021-00743-z

Biello, D., 2011. Green Energy's Big Challenge: The Daunting Task of Scaling Up.

Binner, J., Vaidhyanathan, B., Wang, J., Price, D., Reading, M., 2007. Evidence for Non-Thermal Microwave Effects Using Single and Multimode Hybrid Conventional/Microwave Systems. Journal of Microwave Power and Electromagnetic Energy 42, 47–63. https://doi.org/10.1080/08327823.2007.11688583

Bonifas, C.J., Marconnet, A., Booske, J.H., Cooper, R.F., 2007. Microwave-Induced Mass Transport Enhancement in Nano-Porous Aluminum Oxide Membranes. Journal of Microwave Power and Electromagnetic Energy 42, 13–22. https://doi.org/10.1080/08327823.2007.11688576

Bussi, G., Zykova-Timan, T., Parrinello, M., 2009. Isothermal-isobaric molecular dynamics using stochastic velocity rescaling. The Journal of Chemical Physics 130, 074101. https://doi.org/10.1063/1.3073889

Butler, R.M., Mcnab, G.S., Lo, H.Y., 1981. Theoretical studies on the gravity drainage of heavy oil during in-situ steam heating. Can J Chem Eng 59, 455–460. https://doi.org/10.1002/cjce.5450590407

Chen, J., Warner, M.J., Sikora, B., Kiddle, D., Coverdell, D., Allam, O., Kohl, P.A., Jang, S.S., 2023. The selective heating effect of microwave irradiation on a binary mixture of water and polyethylene oxide: a molecular dynamics simulation approach. Phys. Chem. Chem. Phys. 25, 12522–12531. https://doi.org/10.1039/D3CP00349C

Chen, Q., Liu, Q., 2019. Bitumen Coating on Oil Sands Clay Minerals: A Review. Energy Fuels 33, 5933–5943. https://doi.org/10.1021/acs.energyfuels.9b00852

Cheng, Y., Yuan, S., 2020. Emulsification of Surfactant on Oil Droplets by Molecular Dynamics Simulation. Molecules 25, 3008. https://doi.org/10.3390/molecules25133008

Chung, T., Bae, W., Lee, J., Lee, W., Jung, B., 2011. A Review of Practical Experience and Management of the SAGD Process for Oil Sands Development. Energy Sources, Part A: Recovery, Utilization, and Environmental Effects 34, 219–226. https://doi.org/10.1080/15567030903551224

Clark, K.A., 1966. . Can. Petrol. 7, 18–25.

Cui, G., Liu, T., Xie, J., Rong, G., Yang, L., 2022. A review of SAGD technology development and its possible application potential on thin-layer super-heavy oil reservoirs. Geoscience Frontiers 13, 101382. https://doi.org/10.1016/j.gsf.2022.101382

Dick, T.J., Madura, J.D., 2005. Chapter 5 A Review of the TIP4P, TIP4P-Ew, TIP5P, and TIP5P-E Water Models, in: Annual Reports in Computational Chemistry. Elsevier, pp. 59–74. https://doi.org/10.1016/S1574-1400(05)01005-4

Dodda, L.S., Cabeza de Vaca, I., Tirado-Rives, J., Jorgensen, W.L., 2017a. LigParGen web server: an automatic OPLS-AA parameter generator for organic ligands. Nucleic Acids Research 45, W331–W336. https://doi.org/10.1093/nar/gkx312

Dodda, L.S., Vilseck, J.Z., Tirado-Rives, J., Jorgensen, W.L., 2017b. 1.14*CM1A-LBCC: Localized Bond-Charge Corrected CM1A Charges for Condensed-Phase Simulations. J. Phys. Chem. B 121, 3864–3870. https://doi.org/10.1021/acs.jpcb.7b00272

English, N.J., 2006. Molecular dynamics simulations of microwave effects on water using different long-range electrostatics methodologies. Molecular Physics 104, 243–253. https://doi.org/10.1080/14733140500352322

English, N.J., MacElroy, J.M.D., 2003a. Hydrogen bonding and molecular mobility in liquid water in external electromagnetic fields. The Journal of Chemical Physics 119, 11806–11813. https://doi.org/10.1063/1.1624363

English, N.J., MacElroy, J.M.D., 2003b. Molecular dynamics simulations of microwave heating of water. The Journal of Chemical Physics 118, 1589–1592. https://doi.org/10.1063/1.1538595

English, N.J., Waldron, C.J., 2015. Perspectives on external electric fields in molecular simulation: progress, prospects and challenges. Phys. Chem. Chem. Phys. 17, 12407–12440. https://doi.org/10.1039/C5CP00629E

Fehske, H., Schneider, R., Weiße, A. (Eds.), 2008. Computational Many-Particle Physics, Lecture Notes in Physics. Springer Berlin Heidelberg, Berlin, Heidelberg. https://doi.org/10.1007/978-3-540-74686-7

Gao, F., Shao, Y., Zhou, K., 2020. Analysis of Microwave Thermal Stress Fracture Characteristics and Size Effect of Sandstone under Microwave Heating. Energies 13, 3614. https://doi.org/10.3390/en13143614

Gautam, B., 2021. Energy Minimization, in: Trindade Maia, R., Maciel De Moraes Filho, R., Campos, M. (Eds.), Homology Molecular Modeling - Perspectives and Applications. IntechOpen. https://doi.org/10.5772/intechopen.94809

Graham, R.J., Helstrom, J.J., Mehlberg, R.L., 1987. Solvent Extraction Process for Tar Sand. Presented at the Proceedings of Oil Shale Symposium, Lexington, KY.

Grubmüller, H., Heller, H., Windemuth, A., Schulten, K., 1991. Generalized Verlet Algorithm for Efficient Molecular Dynamics Simulations with Long-range Interactions. Molecular Simulation 6, 121–142. https://doi.org/10.1080/08927029108022142

Guo, Y.-W., Qin, J.-Y., Hu, J.-H., Cao, J.-H., Zhu, Z., Wang, C.-L., 2020. Molecular rotation-caused autocorrelation behaviors of thermal noise in water. NUCL SCI TECH 31, 53. https://doi.org/10.1007/s41365-020-00767-w

Guzik, P., Kulawik, P., Zając, M., Migdał, W., 2022. Microwave applications in the food industry: an overview of recent developments. Critical Reviews in Food Science and Nutrition 62, 7989–8008. https://doi.org/10.1080/10408398.2021.1922871

Hoogenboom, R., Wilms, T.F.A., Erdmenger, T., Schubert, U.S., 2009. Microwave-Assisted Chemistry: a Closer Look at Heating Efficiency. Aust. J. Chem. 62, 236. https://doi.org/10.1071/CH08503

Horn, H.W., Swope, W.C., Pitera, J.W., Madura, J.D., Dick, T.J., Hura, G.L., Head-Gordon, T., 2004. Development of an improved four-site water model for biomolecular simulations: TIP4P-Ew. The Journal of Chemical Physics 120, 9665–9678. https://doi.org/10.1063/1.1683075

Hristova, E., Nikooyeh, K., Stoyanov, S.R., 2023. Water Separation Performance in Bitumen Recovery from Athabasca Oil Sands: Implementation of Separation Efficiency Index. Energy Fuels 37, 7648–7656. https://doi.org/10.1021/acs.energyfuels.2c03547

Internationale Energieagentur (Ed.), 2010. World energy outlook 2010, World Energy Outlook. Paris.

Jensen, F., 2017. Introduction to computational chemistry, Third edition. ed. Wiley, Chichester, UK ; Hoboken, NJ.

Jordaan, S.M., 2012. Land and Water Impacts of Oil Sands Production in Alberta. Environ. Sci. Technol. 46, 3611–3617. https://doi.org/10.1021/es203682m

Jorgensen, W.L., Maxwell, D.S., Tirado-Rives, J., 1996. Development and Testing of the OPLS All-Atom Force Field on Conformational Energetics and Properties of Organic Liquids. J. Am. Chem. Soc. 118, 11225–11236. https://doi.org/10.1021/ja9621760

Jorgensen, W.L., Tirado-Rives, J., 2005. Potential energy functions for atomic-level simulations of water and organic and biomolecular systems. Proc. Natl. Acad. Sci. U.S.A. 102, 6665–6670. https://doi.org/10.1073/pnas.0408037102

Khalkhali, R., Peyravi, A., Hashisho, Z., Choi, P., 2022. Microwave-Assisted Removal of Cyclohexane from Oil Sands Gangue. Ind. Eng. Chem. Res. 61, 6611–6617. https://doi.org/10.1021/acs.iecr.2c00224

Komarov, V., Wang, S., Tang, J., 2005. Permittivity and Measurements, in: Chang, K. (Ed.), Encyclopedia of RF and Microwave Engineering. Wiley. https://doi.org/10.1002/0471654507.eme308

Leadbeater, N.E., 2014. 9.10 Organic Synthesis Using Microwave Heating, in: Comprehensive Organic Synthesis II. Elsevier, pp. 234–286. https://doi.org/10.1016/B978-0-08-097742-3.00920-4

Lemak, A.S., Balabaev, N.K., 1994. On The Berendsen Thermostat. Molecular Simulation 13, 177–187. https://doi.org/10.1080/08927029408021981

Lin, F., Stoyanov, S.R., Xu, Y., 2017. Recent Advances in Nonaqueous Extraction of Bitumen from Mineable Oil Sands: A Review. Org. Process Res. Dev. 21, 492–510. https://doi.org/10.1021/acs.oprd.6b00357

Matsumoto, M., Matsuura, T., 2004. Molecular Dynamics Simulation of a Rising Bubble. Molecular Simulation 30, 853–859. https://doi.org/10.1080/08927020412331317467

Meadus, F.W., Chevrier, P.J., Sparks, B.D., 1982. . Fuel Processing Technology 6, 277–287.

Mohorič, T., Bren, U., 2020. How does microwave irradiation affect the mechanism of water reorientation? Journal of Molecular Liquids 302, 112522. https://doi.org/10.1016/j.molliq.2020.112522

OIL SANDS MAGAZINE, 2020. OIL SANDS GEOLOGY AND THE PROPERTIES OF BITUMEN. OIL SANDS MAGAZINE.

OIL SANDS MAGAZINE, 2016. MINING VERSUS IN-SITU: A LOOK AT HOW ENERGY COMPANIES ARE SHIFTING THEIR PRIORITIES.

Parrinello, M., Rahman, A., 1981. Polymorphic transitions in single crystals: A new molecular dynamics method. Journal of Applied Physics 52, 7182–7190. https://doi.org/10.1063/1.328693

Peng, J., Li, Z., Drakeford, B.M., 2020. Dynamic Characteristics of Crude Oil Price Fluctuation—From the Perspective of Crude Oil Price Influence Mechanism. Energies 13, 4465. https://doi.org/10.3390/en13174465

Piyasena, P., Dussault, C., Koutchma, T., Ramaswamy, H.S., Awuah, G.B., 2003. Radio Frequency Heating of Foods: Principles, Applications and Related Properties—A Review. Critical Reviews in Food Science and Nutrition 43, 587–606. https://doi.org/10.1080/10408690390251129

Rapaport, D.C., 2004. The Art of Molecular Dynamics Simulation, 2nd ed. Cambridge University Press. https://doi.org/10.1017/CBO9780511816581

Shi, H., Huang, K., Liu, Y., Gou, D., 2023. Multidirectional Polarization Impacts on Microwave Heating Efficiency: A Molecular Dynamics Research of Microwave Heating of Common Solvents. J. Phys. Chem. B 127, 970–979. https://doi.org/10.1021/acs.jpcb.2c07548

Sparks, B.D., Meadus, F.W., 1981. A study of some factors affecting solvent losses in the solvent extraction — spherical agglomeration of oil sands. Fuel Processing Technology 4, 251–264. https://doi.org/10.1016/0378-3820(81)90002-3

Van Der Spoel, D., Lindahl, E., Hess, B., Groenhof, G., Mark, A.E., Berendsen, H.J.C., 2005. GROMACS: Fast, flexible, and free. J. Comput. Chem. 26, 1701–1718. https://doi.org/10.1002/jcc.20291

Van Gunsteren, W.F., Berendsen, H.J.C., 1990. Computer Simulation of Molecular Dynamics: Methodology, Applications, and Perspectives in Chemistry. Angew. Chem. Int. Ed. Engl. 29, 992–1023. https://doi.org/10.1002/anie.199009921

Wang, D., Zhao, Z., Qiao, C., Yang, W., Huang, Y., McKay, P., Yang, D., Liu, Q., Zeng, H., 2020. Techniques for treating slop oil in oil and gas industry: A short review. Fuel 279, 118482. https://doi.org/10.1016/j.fuel.2020.118482

Wu, J., Dabros, T., 2012. Process for Solvent Extraction of Bitumen from Oil Sand. Energy Fuels 26, 1002–1008. https://doi.org/10.1021/ef201457m

Zhu, Y., Yan, C., Liu, Q., Masliyah, J., Xu, Z., 2018. Biodiesel-Assisted Ambient Aqueous Bitumen Extraction (BA3BE) from Athabasca Oil Sands. Energy Fuels 32, 6565–6576. https://doi.org/10.1021/acs.energyfuels.8b00688